



# Seismic High-Resolution Acquisition Electronics for the NASA InSight Mission on Mars

Peter Zweifel, Davor Mance, Jan ten Pierick, Domenico Giardini, Cedric Schmelzbach, Thomas Haag, Tobias Nicollier, Savas Ceylan, Simon Stähler, Martin van Driel, et al.

## ► To cite this version:

Peter Zweifel, Davor Mance, Jan ten Pierick, Domenico Giardini, Cedric Schmelzbach, et al.. Seismic High-Resolution Acquisition Electronics for the NASA InSight Mission on Mars. Bulletin of the Seismological Society of America, 2021, 111 (6), pp.2909-2923. 10.1785/0120210071 . hal-03917211

**HAL Id: hal-03917211**

**<https://u-paris.hal.science/hal-03917211>**

Submitted on 23 Sep 2023

**HAL** is a multi-disciplinary open access archive for the deposit and dissemination of scientific research documents, whether they are published or not. The documents may come from teaching and research institutions in France or abroad, or from public or private research centers.

L'archive ouverte pluridisciplinaire **HAL**, est destinée au dépôt et à la diffusion de documents scientifiques de niveau recherche, publiés ou non, émanant des établissements d'enseignement et de recherche français ou étrangers, des laboratoires publics ou privés.

# Seismic High-Resolution Acquisition Electronics for the NASA InSight Mission on Mars

P. Zweifel<sup>1,\*</sup>, D. Mance<sup>1</sup>, J. ten Pierick<sup>1</sup>, D. Giardini<sup>1</sup>, C. Schmelzbach<sup>1</sup>, T. Haag<sup>1</sup>, T. Nicollier<sup>6</sup>,  
S. Ceylan<sup>1</sup>, S. Stähler<sup>1</sup>, M. van Driel<sup>1</sup>, D. Sollberger<sup>1</sup>, F. Euchner<sup>1</sup>, J.F. Clinton<sup>1</sup>, M. Bierwirth<sup>2</sup>,  
M. Eberhardt<sup>2</sup>, P. Lognonné<sup>3</sup>, W.T. Pike<sup>4</sup>, W.B. Banerdt<sup>5</sup>

\* Corresponding author: Peter Zweifel, Institute of Geophysics, ETH Zurich, c/o Schachenstrasse  
39a, 8633 Wolfhausen, Switzerland, +41 79 572 85 82, [peter.zweifel@retired.ethz.ch](mailto:peter.zweifel@retired.ethz.ch)

<sup>1</sup> Eidgenössische Technische Hochschule Zürich

<sup>2</sup> Max-Planck-Institute for Solar System Research, Göttingen

<sup>3</sup> Institut de Physique du Globe de Paris

<sup>4</sup> Imperial College London

<sup>5</sup> Jet Propulsion Laboratory / California Institute of Technology

<sup>6</sup> Eidgenössische Forschungsanstalt WSL, Birmensdorf

## Declaration of Competing Interests

The authors acknowledge there are no conflicts of interest recorded.

## Abstract

The InSight (Interior exploration using Seismic Investigations, Geodesy and Heat Transport)  
seismometer instrument SEIS (Seismic Experiment for Interior Structure) was deployed on Mars  
in December 2018 and went into scientific operation mode starting from March 2019. The

Acquisition and Control electronics (AC) is a key element of SEIS. The AC acquires the seismic signals of the two sets of seismic sensors with high resolution, stores the data in its local non-volatile memory for later transmission by the lander and controls the numerous functions of SEIS. In this paper, we present an overview of the AC with its connections to the sensors and to the lander, as well as its functionality. We describe the elements of the acquisition chains and filters, and discuss the performance of the seismic and temperature channels. Furthermore, we outline the safety functions and health monitoring, which are of paramount importance for reliable operation on Mars. In addition, we analyze an artefact affecting the seismic data referred to as the ‘tick-noise’, and provide a method to remove this artefact by post-processing the data.

## Introduction

NASA InSight landed on Mars on November 26, 2018 (Banerdt et al., 2020). The InSight lander is equipped with three instruments:

- SEIS: consisting of a very broadband (VBB) and one short period (SP) seismometer each with three components (P. Lognonné, 2019)
- HP<sup>3</sup>: Heat Flow and Physical Properties Package (Spohn et al., 2018)
- RISE: Rotation and Interior Structure Experiment (Folkner et al., 2018)

SEIS is the primary instrument of the mission. Between December 2018 and March 2019, after initial operation of the lander, SEIS was commissioned, configured and deployed on the surface of Mars, and then began scientific operation.

SEIS consists of three main parts:

- the Sensor Assembly (SA), which was placed on the ground by the InSight’s robotic arm
- the Electronics Box (E-Box), which resides in the temperature-controlled lander compartment, called the Warm Electronics Box (WEB)

- the tether connecting the SA to the E-Box

The SA incorporates the seismic sensors, the leveling mechanism and a thermal protection (Figure 1). Three identical, oblique-oriented VBB sensor axes are located in a vacuum sphere and mounted on the ring-shaped leveling structure (LVL). Each VBB sensor has a proximity electronics attached to the LVL. One vertical and two horizontal SP sensors are fixed on the outer side of LVL separated at angles of 120 degrees. The LVL has three extendable legs, which can be adjusted in order to level the SA on a slope of up to 15 degrees. (A detailed description of the SEIS instrument can be found in (P. Lognonné, 2019)).

There are temperature sensors installed on each of the VBB and SP sensors, in the VBB proximity electronics and on the structure. The latter is used to measure the SA temperature with high resolution for decorrelation purposes. Each VBB sensor includes a motor driven mass centering and a temperature compensation mechanism. The LVL is equipped with motors to move the legs, supported by coarse and high-precision tilt-meters. Heaters are attached to the inner side of the LVL ring to keep the SA temperature above  $-65^{\circ}\text{C}$  and thus within the safe operating temperature range. A double-walled thermal enclosure (RWEB) covers and protects the entire SA. After deployment on ground, a Wind and Thermal Shield (WTS) is placed over the SA to complete the protection and insulation of the sensitive sensors.

The tether is the electrical connection between the SA and the E-Box. It is a 3 m long semi-rigid, layered flat cable (partially visible in Figure 1) carrying about 200 wires for the sensor signals, power and ground connections, control signals, measurement signals, motor drive lines for leveling, mass-centering, etc.

Here, we give a brief description of the SEIS electronics. We then describe the seismic data acquisition channels and processing chain. We present the acquisition performance of the seismic and the temperature channels. Finally, we describe an artefact caused by the electronics,

which we refer to as the “tick noise”, and provide a method of removing it from the seismic dataset.

### SEIS Electronics

The E-Box comprises all SEIS electronics, except the VBB proximity electronics, some electronics inside the SP sensors and the high precision tiltmeter front end electronics mounted on the LVL. The E-Box is located in a triangle-shaped space in the WEB, hanging upside down below the lander deck. The WEB contains most of the lander and instrument electronics and is heated to prevent temperatures to fall below -35 °C. The picture in Figure 2 shows the E-Box Flight Model (FM) unit in preparation for the thermal test.

The E-Box is implemented as a modular structure and includes all SEIS boards (see exploded view in Figure 2):

- Power distribution and conditioning electronics (DC), two boards
- Acquisition electronics (ACQ), one board
- Control electronics (CTL), two boards
- VBB Feedback electronics VBB-FB[123], three boards
- SP Feedback electronics SP-FB, one board for all three axes
- Leveling Motor Drive Electronics LVL-MDE, one board

The Acquisition and Control electronics (AC) consists of the ACQ, CTL and DC boards. It constitutes a sophisticated seismic data logger that provides, besides the high-resolution acquisition of seismic sensors, the power for the instrument and a variety of functions to run the instrument fully remote controlled in the environment of Mars as described later in this paper. It is the core of the SEIS instrument and provides interfaces to the Command & Data Handling Unit (C&DH) and Power Distribution & Drive Unit (PDDU) on the lander side, and to the instrument’s sub-systems (VBB and SP sensors, LVL).

95 Since SEIS is the primary instrument of the InSight mission, reliability is paramount. The  
96 instrument has to withstand "single-point failures". This is accomplished by duplicating vital  
97 parts of the instrument. The two sensor packages (VBB and SP) with their associated electronics  
98 meet this requirement, since an SP sensor can replace a defective VBB sensor to a certain extent  
99 and vice versa. Their associated electronics consist of the sensor feedback electronics and the  
100 acquisition front-end circuits of the AC, with the latter providing signal conditioning and the  
101 analog-to-digital conversion.

102 The AC, which is the central part of the instrument, is duplicated except for the aforementioned  
103 front-end circuitry and the LVL-MDE electronics. This means that there are two identical  
104 electronics, called the A-side and B-side of the AC. In the event of a fault, the B-side can  
105 substitute the defective A-side or vice versa. The A-side is used for nominal operation. The  
106 sensor and associated electronics as well as the LVL-MDE are connected to both sides of the  
107 AC. The PDDU supplies the SEIS instrument with four +28 V primary power lines. Two of  
108 these lines are connected to the A-side and two to the B-side of the AC. The C&DH (likewise  
109 duplicated) controls the PDDU switches so that one of the four power lines is powered-up,  
110 activating the corresponding A or B side of the AC.

111 The LVL MDE board is not duplicated due to volume and mass constraints in the WEB and  
112 limitations on the number of wires in the cable. The associated risk is considered acceptable  
113 because sensor leveling is rarely used and is only activated when temperatures are highest on  
114 Mars.

115 As a further safety measure, each sensor-axis can be switched off individually to isolate  
116 defective sensors or circuits. Automatic over-current protection circuits switch off parts or all of  
117 the electronics. To detect potential problems or adverse trends, numerous housekeeping channels  
118 measure currents, voltages and temperatures in the various instrument parts. The housekeeping

data is stored and downlinked to Earth for health monitoring by the instrument operation engineers.

The block diagram in Figure 2 shows the main connections within the SEIS instruments to the spacecraft and to the Auxiliary Payload Sensor Suite (APSS) (see Banfield, 2018). The DC boards convert the primary power into several positive and negative supply voltages required by the AC and the sub-systems. The duplicated interfaces to the lander computers C&DH A and C&DH B are cross-strapped and consist of a low speed serial line for commands and special data, and a serial 4 Mbit/s line for the high-speed transmission of acquired sensor and health data to the lander for further processing or downlink to Earth.

The SEIS command dictionary incorporates eighty commands with various parameters to cover all functions of the SEIS instrument, such as turning on sub-systems, starting/stopping the acquisition, configuring sampling rates and gains, retrieving specific data, and so on. The APSS receives a 1-second pulse from SEIS. This pulse is used to time-correlate the APSS data with SEIS data.

#### Seismic Acquisition Channels

There are nine seismic acquisition channels. The VBB sensors provide three velocity and three position signals, the SP sensors three velocity signals. Each of these signals is digitized by a dedicated 24-bit sigma-delta Analog-to-Digital Converter (ADC) and then filtered, time-stamped and stored in the on-board non-volatile memory. The lander computer C&DH retrieves the data regularly and then processes and stores the data in its mass memory. The acquired and processed data can then be downlinked to Earth on request.

## Acquisition Chain

The acquisition chain consists of the conditioning electronics (amplifier/filter), the ADC and the Finite Impulse Filter (FIR; see block diagram in Figure 3). The conditioning electronics in front of the ADC scales the seismic signals from the sensor full-scale range to the input voltage range of the ADC. The full-scale ranges are  $\pm 25$  Volt for the VBBs (for both velocity and position signals) and  $\pm 12.5$  Volt for the SP velocity signals. In addition, the conditioning electronics filters the signal by the second-order low pass filter, which is the first part of a 3-step anti-aliasing filter. To reduce the low frequency ( $1/f$ ) noise, low offset, zero drift (auto zero) amplifiers are used.

## Analog-to-Digital Conversion

The performance requirement “seismic signals with a dynamic range of at least 130 dB in amplitude” require the use of a 24-bit ADC. At the time the InSight development began in 2012, 24-bit ADC’s were state-of-the-art in seismic data loggers and in industry in general, but not common in space projects. The challenge for these rather complex integrated circuits is to sustain the impact of cosmic radiation in space when departing the protective magnetosphere of Earth, and after landing on Mars. The 24-bit sigma-delta ADC AD7712 was finally selected for SEIS due to its robustness with respect to radiation and its availability in MIL quality (military temperature range and ceramic packaging). The device passed the radiation tests without any permanent destruction although it showed some malfunctions that altered configuration registers and interrupted the conversion. These failure conditions are managed in operation by monitoring and rewriting the ADC’s configuration registers.

The ADC converts the signals with an input sampling rate of 32 kHz. The on-chip 3<sup>rd</sup> order sinc-in-time filter ( $\text{sinc}^3$ ) is followed by a decimation by a factor of 64 for the velocity channels and by a factor of 3200 for the position channels. The corresponding ADC output rates are thus



165 500 Hz for VBB and SP velocity and 10 Hz for VBB position. This  $\text{sinc}^3$  filter constitutes the  
166 second stage of the anti-aliasing filtering.

#### 167 FIR Filter

168 The FIR filters, implemented in the Field Programmable Gate Array (FPGA), apply a sharp low-  
169 pass filter, which allows decimating the filter output data to the final output rates. For the VBB  
170 and SP velocity channels, a sampling rate of 100 Hz or 20 Hz is selectable. The upper diagram in  
171 Figure 4 shows the corresponding filter layout. If 100 Hz data is selected, only stage 1 is used,  
172 i.e., the output samples of stage 1 will end up in the data packet. If 20 Hz data is selected, both  
173 stages are used and the output samples of stage 2 will end up in the data packet.

174 For the VBB position and Scientific Temperature SCIT (LVL temperature) channels, the  
175 sampling rates of 1 Hz and 0.1 Hz are available. The corresponding filter layout is shown in the  
176 lower diagram in Figure 4.

177 The FIR filter is the third and last stage of the anti-aliasing filtering. The standard filter used for  
178 seismic recordings is identical to the terrestrial broadband seismological station CLPFO (refer to  
179 P. Lognonné, 2019).

180 The data samples of the seismic and the temperature channels are buffered and then 1-second  
181 data packets are constructed from them. These packets are time-stamped with the Local On-  
182 Board Time (LOBT) that corresponds to the instant when the first sample of the 1-second data  
183 packet was acquired. The packets are stored in the FLASH memory, which can hold more than  
184 65 hours of data. The FLASH memory is organized as a ring buffer; i.e., as soon as the memory  
185 is filled-up, the oldest data is overwritten.

#### 186 Anti-aliasing Filter

187 The resulting anti-aliasing filter is the product of the three filter steps mentioned in the previous  
188 sections. The first two steps are implemented as hardware, only the FIR filter in FPGA can be

configured. Figure 3 left side shows the individual attenuation of each of the three filter steps up to 600 Hz.

It can be seen that the FPGA filters do not suppress signals with a frequency of  $500 \text{ Hz} \pm 8 \text{ Hz}$ , as these signals appear in the pass band due to folding around the ADC Nyquist frequency of 250 Hz. However, this effect coincides with the notch of the ADC filters at 500 Hz. Therefore, the total attenuation of the cascaded filters remains at almost 120 dB for frequencies above the pass band (see Figure 3 right hand side). The contribution of the analog filter (first filter step) is less than 10 dB in the frequency range shown.

#### FIR Filter upload

The FIR filter coefficients can be uploaded from Earth via the lander and changed for certain channel groups. Channel groups are VBB velocity channels, SP velocity channels, VBB position channels and the SCIT channel. This capability is used to change filters for special purposes, as for example, to achieve an extended bandwidth as described in the section ‘Strategies to record information beyond the Nyquist frequency of 50 Hz’.

#### Channel Noise Performance

The acquisition noise is a result of the amplifier noise of the signal conditioning, the intrinsic noise of the ADC and the voltage reference noise (Figure 5). The ADC intrinsic noise of  $3.8 \mu\text{V}/\sqrt{\text{Hz}}$  is flat (white) down to 10 mHz, below which the ADC  $1/f$  noise becomes visible. Above about 8 Hz, the ADC quantization noise starts to dominate over the ADC white noise and becomes therefore visible at 100 Hz data rate up to the FIR filter corner frequency of 40 Hz. A space qualified external voltage reference (RH1021-5), with a temperature sensitivity of  $<5 \text{ ppm/K}$  is used to achieve good stability. It has a low noise, matching the ADC performance. The acquisition noise level at low frequencies ( $<100 \text{ mHz}$ ) depends on the input signal amplitude since the voltage reference noise is proportionally scaled with the acquired signal. For signals

less than about 25% of the full-scale range (FSR), the voltage reference noise is not significant w.r.t. the intrinsic noise of ADC (Figure 5). For the 20 Hz data rate, the FIR filter with 8 Hz corner frequency will completely attenuate the quantization noise. (See also P. Lognonné et al, 2019)

#### Measured VBB channel performance

To illustrate the measured performance of the acquisition system, we compare the electrical noise of the acquisition channels obtained during the electrical tests with the seismic noise recorded during a very quiet period on Mars. The results are displayed in  $V/\sqrt{\text{Hz}}$  (amplitude spectrum density) and are referred to the inputs of the acquisition system.

When the E-Box is fully assembled, the inputs of the recording system are not accessible anymore. Therefore, we present noise results recorded during the electronics tests before integration of the sensor feedback electronics, i.e., during the so-called board level tests in the manufacturing phase. The test configuration only includes the AC part of the E-Box (see section ‘SEIS Electronics’). The corresponding spectra in the diagrams are labeled "Channel AC". The noise requirement for the acquisition channels is shown with the red line.

The right panel in Figure 6 shows the VBB velocity channels recorded with a sampling rate of 100 Hz. The Mars data was acquired on 2020-02-04 at 17:52 for 15 min (between 21:00-22:00 on Sol 423 – an extremely quiet time with minimal wind noise). The tick-noise artefact was removed from the Mars data (the tick-noise and the removal procedure is described in detail in section ‘1-Hz Mode (Tick-noise)’). In addition to the VBB sensor data, the acquisition system data, in which the sensor noise is not present, was acquired prior to the mission on 2014-10-16 for 15 min during the board level test of the FM electronics. The acquisition noise corresponds to the ADC intrinsic noise as shown in Figure 5 up to about 8 Hz. The ADC quantization noise

becomes dominant above 8 Hz and increases up to the corner frequency of the FIR filter, as explained in the section above.

In the left panel of Figure 6, VBB position channels with a sampling frequency of 1 Hz are compared. The Mars data was acquired on 2019-10-18 at 20:00 for 59 min, while the acquisition system data was recorded on 2014-10-04 for 59 min. Above ~0.15 Hz, the sensor noise becomes equal to or smaller than the acquisition noise.

#### Measured SP channel performance

The acquisition channels for the SP are identical to the VBB channels except that the full-scale range is reduced by half to  $\pm 12.5\text{V}$ . Therefore, the noise limit is lowered accordingly. Figure 7 shows the horizontal SP channels recorded during cruise on 2018-07-16 at 15:48 for 7 min and all three SP channels on Mars (2019-01-12 at 05:10 for 15 min), as well as the recorded acquisition channels during instrument board level test of the FM electronics on 2014-10-16 for 15 min, all with sampling frequency of 100 Hz. The cruise recordings show only the horizontal SP sensors as they work well in zero gravity environment. In contrast, the vertical SP sensor requires gravity to function. The shown noise spectra of the two horizontal SP sensors correspond to their self-noise, as there is no source of vibration on the spacecraft during cruise phase.

As explained in section ‘Channel Noise Performance’, and therefore expected, the ADC quantization noise dominates the acquisition noise above 8 Hz.

#### Linearity (INL)

As part of an instrument performance campaign, the Integral Non-Linearity (INL) of the acquisition channels on the flight spare (exact duplicate of the flight unit on Mars) was measured. A defined precise voltage  $V_{\text{ref}}$  was applied in steps to the differential inputs of the VBB channels (see block diagram in Figure 8). The voltages were acquired by the acquisition

electronics AC and additionally measured by a high-precision Digital Multi-Meter (DMM) to obtain a better knowledge about the input voltage. The measurements were carried out for all VBB channels before feedback board integration. For each tested input voltage, 10 seconds of data were sampled from all VBB channels at the highest sampling rate (i.e., 100 Hz for the velocity channels and 1 Hz for the position channels). The DMM was configured at fixed input range to maintain stable gain and offset during the test.

The analysis of the results was done separately for each VBB channel. First, the straight line between the range end-points is determined by calculating a gain and an offset, such that the digital number returned for the channel relates to the input voltage as follows:

1)

$$VBBchan = gain * V_{input} - offset$$

The offset and gain are determined by the following formulae:

2)

$$gain = \frac{VBBchan(20V) - VBBchan(-20V)}{V_{input}(20V) - V_{input}(-20V)}$$

3)

$$offset = VBBchan(-20V) - gain * V_{input}(-20V)$$

where the values between parentheses are the applied voltage.  $V_{input}$  refers to the value measured with the DMM. The endpoints of -20 V and +20 V correspond to the specified input voltage range.

For each input voltage set, the error is calculated:

4)

$$\varepsilon = VBBchan - gain * V_{input} - offset$$

The INL in percentage of the full-scale range using the maximum error measured, called  $\varepsilon_{max}$ :

5)

$$INL = 100 * \frac{\varepsilon_{max}}{VBBchan(20V) - VBBchan(-20V)}$$

Figure 8 shows the measured errors for all VBB channels for the specified range extended by 10%, from which can be seen that the acquisition is still linear for signals slightly beyond the specified range.

The highest INL measured is about  $3.2 \cdot 10^{-4}$  % for the VBB1 velocity channel, and this is well below  $15 \cdot 10^{-4}$  %, the maximum INL in the ADC (AD7712) specification. A typical INL of  $3 \cdot 10^{-4}$  % is specified for the ADC, and the results for all channels are close to this value. The non-linearity measured is according to what can be expected from the ADC. Thus, no significant contribution from the conditioning electronics is observed. However, we are also at the limits of the measurement setup itself. Therefore, the non-linearity observed may not only reflect the performance of the acquisition system, but also include limitations of the instrumentation and the setup used to obtain the result.

## Temperature Acquisition Channels

There are three temperature measurement systems in the SEIS instrument:

- Scientific Temperature (SCIT A&B): Two thermistors (PT1000) mounted on the ring of the leveling structure. There are two, SCIT A and SCIT B, each connected to the corresponding AC side.
- VBB Engineering Temperature: Three thermistors, mounted on the three VBB sensors providing the sensor temperature
- Housekeeping Temperatures

305 *Scientific Temperature (SCIT)*

306 The SCIT is the tenth high-resolution channel of AC with a dedicated 24-bit ADC. Like the VBB  
307 POS channels, the SCIT is digitized with 32 kHz sample rate and provides, after ADC filtering  
308 and FIR filtering of the FPGA, the output rates of 1 Hz or 0.1 Hz. This high precision  
309 temperature measurement is implemented as a 4-wire measurement, meaning the two excitation  
310 lines to the thermistor are separated from the two sensing lines, to avoid voltage drop affecting  
311 the measurement due to long wires. Figure 9 shows the time-series (left) and the Amplitude  
312 Spectrum Density (ASD) (right) of measurements made during final testing of the E-Box FM  
313 electronics. In order to assess the performance of the circuit using a stable input signal, a resistor  
314 with a fixed and stable value replaced the temperature sensing thermistor.  
315 The transfer function of the SCIT temperature measurement including the non-linear thermistor  
316 can be found in (P. Lognonné, 2019).

317 *VBB Engineering Temperature (VBB[1,2,3] ENG TEMP)*

318 The VBB engineering temperature measurement is a 2-wire measurement, using the same lines  
319 for excitation and sensing. Unlike the seismic channels and the SCIT that have a dedicated ADC,  
320 the three engineering temperature channels share a single ADC that acquires them in sequence.  
321 A multiplexer scans through all channels and a calibration resistor of 1 k $\Omega$ . For each channel and  
322 the calibration resistor, the ADC acquires 16 samples, which are averaged. In a second step, an  
323 offset compensation is applied with equation (6).

324 6)

325 
$$VBBx_{Temp} = VBBx_{avg} + (RefConst - Cal_{avg})$$

326 
$$VBBx_{Temp} = \text{Engineering Temperature Result for each channel, } x = 1 \dots 3$$

327 
$$VBBx_{avg} = \text{averaged 16 ADC samples for each channel, } x = 1 \dots 3$$

328 
$$RefConst = \text{Reference constant representing 1 k}\Omega$$

329  $Cal_{avg}$  = averaged 16 ADC samples measured on calibration resistor of 1 k $\Omega$

330 In contrary to the SCIT channel that is a continuous stream, the VBB engineering temperature  
331 channels are a series of point measurements. There is no post-filtering as with the SCIT channel.  
332 The noise performance, measured at a sample rate of 1 Hz with a fix resistor, is 1.5 mK/ $\sqrt{\text{Hz}}$   
333 over the frequency band from 0.5 Hz down to 0.01 mHz and is well below the requirement of  
334 3 mK/ $\sqrt{\text{Hz}}$ .

335 The conversion factors including the non-linear thermistor can be found in (P. Lognonné, 2019).

### 336 [Housekeeping Temperatures](#)

337 The housekeeping temperatures are a third category of temperature measurements. They are  
338 designed to provide the temperatures of sensors and electronics boards in the instrument for  
339 diagnostic purposes. They are collected together with the voltage and current measurements with  
340 a resolution of 12-bits.

### 341 [Time Base](#)

342 The acquisition clock is derived from the AC master clock, which is based on the Hybrid Crystal  
343 Oscillator QT625LEM-32.768000MHz QTH U. The acquisition is therefore free-running with  
344 respect to the spacecraft clock and the Universal Time Coordinated (UTC). The oscillator  
345 temperature sensitivity is up to  $\sim 1$  ppm/ $^{\circ}\text{C}$  according manufacturer's temperature sensitivity  
346 curve. The estimated drift is then between -20 ppm and +5 ppm in the maximum temperature  
347 range of -35  $^{\circ}\text{C}$  to +50  $^{\circ}\text{C}$  specified for E-Box. The acquired data is time stamped with the Local  
348 On-Board Time (LOBT), which is derived as well from the master clock. This time is kept by a  
349 40-bit counter with a resolution of 1/1024 s. The value of this counter is included as time stamp  
350 in the 1-second packets.

351 The time correlation between the LOBT and UTC is performed in post-processing. This is done  
352 in two steps. The LOBT is correlated with the spacecraft clock (SCLK). For this purpose, the AC



receives the spacecraft clock SCLK together with a synchronization pulse from the lander. This is used to generate pairs of LOBT/SCLK from the same instant in time, which are retrieved by the lander. Then the SCLK time is correlated with UTC using time pairs from the X-band communication.

### Strategies to record information beyond the Nyquist frequency of 50 Hz

For specific seismic investigations, it is of interest to record seismic signals with a frequency content exceeding the effective bandwidth of 0 - 40 Hz (considering the low-pass -3dB corner) with a Nyquist frequency of 50 Hz dictated by the 100 Hz sampling frequency. For example, the eigen-modes of the LVL show eigen-frequencies >50 Hz (Lognonné et al., 2020). Furthermore, the hammering of the HP<sup>3</sup> mole into the ground to measure a vertical thermal conductivity profile will generate signals > 50 Hz that may allow inferring on elastic properties of the shallow Martian crust (Kedar et al., 2017; Golombek et al., 2018; Brinkman et al., 2019). Changing the FIR filters of stage 1 in the velocity signal acquisition chain (Figure 4 upper diagram) allows recording information outside the effective frequency bandwidth of 0 - 40 Hz.

A straightforward way to extend the bandwidth of SEIS is to exploit the fact that, following the Nyquist sampling theorem, the sampling limitations are not dictated by the maximum frequency, but by the bandwidth of the signal. Any signal that is constrained to a bandwidth of 50 Hz with a minimum frequency of an integer multiple of 50 Hz can therefore be exactly reconstructed when sampled at a sampling rate of 100 Hz. For example, changing the FIR filter of a velocity channel to pass 50 - 100 Hz at stage 1 will lead to the data being aliased once (Figure 10). The original information can then be recovered by re-mapping the information that mapped onto the 0 - 50 Hz band back to the 50 - 100 Hz band, resulting in an effective 200 Hz sampling frequency. If data from both the VBB (recording 0 - 50 Hz) and SP instrument (recording 50 - 100 Hz) are combined, a bandwidth from 0 to approximately 100 Hz can be covered. For technical reasons,

the FIR filters must have a DC gain of 1. Therefore, the FIR filter designed to record the 50 – 100 Hz band needs to exclude frequencies close to 100 Hz and in practice ranges from 56 to 87 Hz (-3dB), resulting in an effective bandwidth when combining both VBB and SP from 0 – 87 Hz with a notch at 50 Hz.

A second approach can be applied to repetitive signals with known characteristics, for which significant constraints apply. It is possible to set up inversion schemes to recover information that is aliased even by a few orders, thereby extending the recording bandwidth significantly beyond 50 Hz. Replacing the nominal FIR filter of stage 1 by a single spike will lead to a filter passing all frequencies (Sollberger et al., 2020). Subsequent down-sampling will result in the information being aliased up to several orders. The original signals can be reconstructed by making use of the fact that the HP<sup>3</sup> hammering waveform data are characterized by a high number of similar signals generated by each mole hit. Additionally, the hammering is not synchronized with the seismic data sampling so that over the repetitions of the signal the samples spread randomly over time, and this allows recovering the full information content up to a sample rate of 500 Hz (Sollberger et al., 2020). The FIR filter coefficients are implemented in the AC as signed 32-bit integer numbers, followed by a scaling of  $2^{-32}$ . The spike filter is realized by setting all coefficients to zero except one that is set to the maximum value resulting in a filter with a gain of  $(2^{31} - 1)/(2^{32}) \approx 0.5$ . Hence, the data acquired while this filter is applied need to be multiplied by a factor of 2 before the usual conversion from digital counts to volts is applied, which results in the loss of 1 bit of resolution (the nominal resolution is 24 bits).

## Health Monitoring and Trend Analysis

Forty-seven housekeeping acquisition channels and numerous status and error flags of E-Box as well as information gathered by the lander provide information about the health of the instrument and especially of the E-Box. If an anomaly occurs, this information can be used to identify and

analyze the problem in order to decide on the corrective action necessary, such as changing the configuration or turning off a sub-system. In addition, by monitoring the health information, adverse trends can be detected before a problem or a defect develops.

The health monitoring gives confidence that the instrument electronics are functioning well. The actual health check system comprises nine current measurements, thirteen voltage measurements, twenty-three temperature measurements, the position measurements of the SP sensors, an analysis of the clock drift, and the evaluation of sixteen error flags and fourteen status flags.

The monitoring system uses state dependent limits, i.e., the limits are set depending on the configuration of the instrument. This allows setting narrower limit bands and provides in addition a check whether the configuration is applied as expected. It significantly reduces the probability of missing anomalous behavior. The configuration of the instrument is determined from the status flags that are returned as part of the health check data.

#### *Trend Analysis*

Trend analyses are performed to analyze the long-term stability of the E-Box. It uses a special version of the health check that shows data from several days at the beginning of the period and several days at the end of the period. This facilitates spotting changes in both the average and spread for the parameters analyzed. Changes in the parameter values due to different configurations that are applied during the reporting interval are taken into account. So far, two reports have been created during the operation on Mars, one for the period from 2019-03-11 to 2019-10-15, and the second for the period from 2019-10-14 to 2020-10-05. The results can be summarized as follows.

*Voltages and Currents:* The configuration changes that are relevant for the E-box voltages and currents during both periods were the switching on and off of the SA heating. The heating was switched on on 2019-05-18. As expected, the current of the + 7V supply increased with the

additional heating current. The heating was switched off on 2020-07-18, which reduced the current again to its initial value. No significant change over time was observed for any other of the currents and voltages.

*Digital status / error flags:* For the status and error flags, a trend analysis is not applicable. The analysis of the error and status flags in the full reports showed that no error flags were triggered in either of the reported periods. This means that no over-currents have occurred that would have resulted in sub-systems being switched off. No samples were marked invalid for any reason other than overflow in one of the FIR stages, which can also occur during FIR filter settling if a channel is activated. Furthermore, no adverse radiation effects on the operational amplifiers used for the conditioning of the seismic sensor signals were encountered. There was no radiation related disruption in the ADC, which is detected and flagged accordingly by the ADC controller, and thus its synchronization and calibration was established and retained throughout the active period.

*Memory data retention:* Only few single-bit errors occurred in the FLASH memory within both periods. The FLASH controller corrects these errors, i.e., they do not result in loss of scientific data. The frequency at which these errors have occurred since landing on Mars is at the expected rate and not increasing. No double-bit errors, which cannot be corrected by the FLASH controller, have occurred in the FLASH memory.

The FIR coefficients were always read before the FIR filters were updated or reconfigured and each time the read coefficients were identical to those previously programmed. Thus, there was no data retention problem for the FIR coefficients.

*LOBT drift versus SCLK:* Figure 11 shows the LOBT drift w.r.t. the SCLK in parts per million for the last reporting period. No significant difference over time is observed, although the negative peaks seem to be more pronounced in the last set of days. This difference correlates

with the temperature of the crystal used for the LOBT. The frequency of this crystal is maximum at 0 °C and thus decreases when the temperature is lower. The temperature's diurnal cycle stays above -15 °C for the first two sets of days, but has minima as low as -20 °C in the last set of days. These lower temperatures explain the more pronounced minima in the last set of days. The maximum drift of the LOBT w.r.t SCLK is around 3.5 ppm in both reporting periods. No significant change over time could be observed. The limits shown in the plot take into account the entire temperature range in which the E-Box can operate, i.e., from -35 °C to +50 °C.

*LVL-MDE communication:* The full reports have shown that communication with the LVL-MDE was always successful in the reported periods. This can be confirmed by the acknowledge messages received from the LVL-MDE.

*Summary:* In both periods, i.e., during the entire scientific operation on Mars, no anomaly or adverse trend was found in the E-Box.

#### 1-Hz Mode (Tick-noise)

The seismic data acquired by the SEIS instrument show a very small but constant 1 Hz signal with its higher harmonic modes (subsequently denoted as “tick-noise”) as an artefact on all the VBB and SP velocity channels. The amplitude of the tick-noise is of order up to fifty  $\mu\text{V}_{\text{rms}}$  at the various acquisition system inputs (referring to a full-scale of  $\pm 12.5$  V for SP and  $\pm 25$  V for VBB). The tick-noise is produced by cross-coupling from switching signals to the sensitive sensor lines that carry the seismic signal, which are routed in parallel through the sensor feedback boards and the 3-meter-long tether down to the sensor assembly. The aggressor signals belong to temperature measurements that are driven by the AC. Currents are being sent through various thermistors in the VBB sensors and their front-end electronics to measure the resulting voltages representing the temperatures. These measurements are cycled through the thermistors,

i.e., the signals are switched to each of the thermistors one after the other, every second. This on-off current switching produces transients on the sensor lines at a 1 s repetition rate, resulting in the observed tick-noise. A detailed investigation on the flight spare acquisition and control electronics confirmed that the shapes of the tick-noise could be traced back to the switching instants of the different temperature measurement channels. The tick-noise is most evident during periods of low seismic noise and appears as peaks in the frequency spectrum or as horizontal lines in spectrograms. The tick noise is also prominent in spectrum density charts of longer measurements, where the frequency bins become very narrow, because all its energy is concentrated in a few bins. Examples of tick-noise are shown in Figure 12 and discussed in more detail in the following section.

#### *Investigation and characterization*

From the beginning of operations on Mars, the tick-noise was monitored as one of the routine health-check tasks of the SEIS instrument. First on a weekly basis, then every month, the VBB and SP velocity signals are stacked and the amplitude spectra calculated. Then they are manually compared with previous stacks. The objective is to identify, over long term, any instability or continuing trend of tick-noise's amplitude or shape. The following information summarizes the findings so far.

In Figure 12 we see the amplitude spectra and in Figure 13 the stacked waveforms of the SEIS velocity channels, recorded in 2019 and 2020 with a 20 Hz sampling rate and configured in high gain, the most common configuration for continuous acquisition on Mars. The left side of Figure 12 shows frequency spectra of the recordings of the three SP channels over 24 hours. The rms (root-mean-square) amplitudes of the tick-noise, calculated from the samples of the stacked signal, vary from channel to channel in the range of 3.9 to 7.5  $\mu\text{V}$ , at a SP full-scale range of  $\pm 12.5\text{ V}$ .

497 Figure 13 left side shows the tick-noise shapes resulting from stacking the signals of SP  
 498 recordings on 2019-07-22, 2020-01-03 and 2020-08-28. The stacked signal is always 1 second  
 499 long, i.e., the number of samples in the stack equals the sampling rate. Note that the peak  
 500 amplitudes do not change significantly over one year's period between the different recordings.  
 501 The shapes and amplitudes of SP1 and SP3 are rather invariant over time. The SP2 has a much  
 502 smaller peak and thus shows larger variation due to the presence of the overall-noise.  
 503 The amplitude spectrum charts in Figure 12 right side show the VBB channels, recorded on  
 504 2020-07-04 over 24 hours. The rms amplitudes of the tick-noise vary from channel to channel  
 505 from  $7.5 \mu\text{V}_{\text{rms}}$  up to  $49 \mu\text{V}_{\text{rms}}$ , the latter due to the significantly larger peak on VBB2. The VBB  
 506 full-scale range is  $\pm 25 \text{ V}$ .  
 507 Figure 13 right side shows stacked VBB waveforms from 2019-06-04, 2020-01-03 and  
 508 2020-07-04. As for the SP channels, the peak amplitudes do not change significantly over one  
 509 year's period between the different recordings. The shape and amplitude of VBB2 is almost  
 510 identical. VBB1 and VBB3 have no distinct peak and show some degree of shape variability, as  
 511 the signal is very small w.r.t. the overall noise.  
 512 The VBB channels configured in low gain are rarely used and only for special purposes.  
 513 Therefore, there are only short records available. To assess how the tick noise affects this  
 514 configuration, waveforms for all three VBB channels were recorded for 40 minutes on  
 515 January 19, 2020. No 1-Hz peaks are visible in the spectra of VBB1 and VBB2 because they fall  
 516 below the noise floor of the sensors. VBB2 shows a peak at 1 Hz, of which the rms amplitude is  
 517  $17.6 \mu\text{V}_{\text{rms}}$ , thus roughly a factor of three smaller than the  $49.2 \mu\text{V}_{\text{rms}}$  of VBB2 in high gain.  
 518 This reflects the gain difference between high and low gain (see P. Lognonné, 2019) and  
 519 indicates that the crosstalk injection point is in front of the gain stage. The gain selection is part  
 520 of the velocity signal output amplifier of the VBB sensor feedback electronics and thus just in

front of the acquisition electronics. In the remaining VBB channel configuration modes, i.e., VBB engineering (ENG) at high and low gain, and SP low gain, the tick-noise is not visible due to the higher sensor noise floor.

In the commissioning phase, the tick-noise appeared as well with a frequency of 0.1 Hz when the temperature measurements were configured to run at a rate of 10 seconds. The effect and root cause is the same as described above. The project decided that this configuration should no longer be used for the science operation of the instrument.

#### *Tick-noise removal*

We suggest removing the tick-noise by subtracting the repetitive 1 Hz signal from the recorded waveform in the time domain. In a first step, we determine the tick-noise waveform by stacking consecutive 1-second chunks from the continuous waveform (i.e., the number of samples per chunk equals the sampling rate). Through this stacking process, the random noise is averaged and thus reduced while the periodic tick-noise is averaged to its amplitude. The result is a waveform of 1 second length, which contains the disturbing tick-noise waveform (see Figure 13).

The stacking process can be expressed in following equation:

7)

$$stackSample(i) = \frac{\sum_{m=0}^{n-1} sample(t+sampleRate*m)}{n}, n = 1 \dots number\ of\ stacks$$

8)

$$number\ of\ stacks = \frac{waveform\ in\ seconds}{sample\ rate}$$

9)

$$Number\ of\ samples\ in\ stacked\ waveform = sampleRate$$

The longer the waveform we are processing, the better the averaging of the random noise and the cleaner the shape of the tick-noise we obtain.



545 In a second step, the offset (i.e., the mean of the samples) is removed from the stacked  
546 waveform, as it is not a part of the disturbing signal.

547 In a third step, this tick-noise waveform is subtracted from the continuous waveform second by  
548 second in exact phase. After subtraction, the resulting waveform is tick-noise free.

549 The waveform correction becomes:

550 10)

551  $corrSample(i) = sample(i) - stackSample(i - sampleRate * m), for m = 0 \dots n - 1$

552 To achieve a successful removal of the tick-noise, one must take into account the following  
553 considerations:

554 a) Use continuous waveforms without gaps

555 b) Subtract exactly in phase, i.e., subtract the stacked waveform from the same 1 second  
556 long chunks that were used in the stacking process

557 c) The quality of the tick-noise removal depends on the averaging process. Although the  
558 suggested tick-noise removal works well with records as short as 20 minutes, longer  
559 waveforms are providing improved results

560 The result of the tick-noise removal works well for most waveforms, including waveforms with  
561 sampling rates of 100 Hz. However, the removal may not work satisfactory on shorter  
562 waveforms with large drift and/or numerous glitches (Scholz et al., 2020). The stacked  
563 waveforms will not be accurate and therefore the tick-noise removal becomes insufficient.

564 Running the removal process on a strongly drifting signal without high-pass filtering results in a  
565 waveform with only slightly reduced tick-noise. Filtering of the waveform before stacking, for  
566 example with a first-order high-pass filter with a corner frequency at 0.1 Hz, leads to an  
567 improved result.

Numerous glitches and strongly varying noise amplitudes prevent the waveform from being averaged properly, making the correction imperfect. A significant improvement can be achieved by using only those data chunks for the stacking process that contain no glitches or only glitches with small amplitudes. This is implemented by calculating the variance of each 1-second chunk and comparing it to a defined threshold value. The threshold has to be found experimentally. In the example in Figure 14, a variance threshold of  $10^{+4}$  was chosen to obtain a more accurate peak shape (chart on the right hand side). Approximately 11% of 2880 data chunks exceeded the threshold and were not used for the stacking process.

Figure 15 shows the resulting waveform with the removed tick-noise. Re-stacking an already "cleaned up" waveform reveals remaining tick noise with an RMS amplitude less than 1 count. This tick-noise residual can be further reduced by applying a dither, i.e., by adding a random fraction of a count to each sample, before writing to the mini seed file. For example, applying a dither of  $\pm 0.5$  count (peak to peak) to the waveform in Figure 15 reduces the remaining tick-noise rms amplitude from 0.29 counts to 0.0073 counts.

Alternative approaches for removing the tick noise could be used, for example, a method in the frequency domain could replace the spectral amplitudes at the peaks with the mean of immediate neighboring frequency bands.

## Conclusions

Electronics development for planetary space projects is challenging. The enormous vibration imposed during launch and the large shocks while landing on the planet mechanically stress the electronics assembly. The performance must be maintained despite the large temperature variations during operations. The space radiation environment outside the protective magnetosphere of Earth can have damaging effects on the electronics components. Limited

power available for planetary missions requires careful balancing and tradeoff between low power design and performance. In order to ensure the successful operation, the requirements with respect to the environment in which the electronics has to perform and sustain are therefore very stringent. The equipment is thoroughly tested before it is accepted for the mission, using temperature ranges that extend well beyond those expected during the real operation. The design must take into account the limited choice of electronics components that are sufficiently thermomechanically robust and radiation tolerant. Compromises were made, such as accepting an increased noise at higher frequencies by selecting the 24-bit ADC for the acquisition that in turn has the required radiation tolerance, which was already proven in flight prior to this mission. SEIS electronics was successfully commissioned and has now been operating for more than two years on Mars without any anomalies, acquiring seismic data with a resolution and a dynamic range that is unprecedented in planetary seismology. The described tick-noise artefact is an unwanted signal that was discovered in the integration phase of the development process, too late to take remedial action. The cause is not a problem of a specific point in the electronics, but rather a problem related to the large instrument layout (acquisition electronics – 3m-tether – sensor assembly). Fortunately, the tick-noise is stable and this paper proposes a method that shows its successful removal by post-processing the data.

609

## 610 [Glossary](#)

611	AC	Acquisition and Control electronics
612	ACQ	Acquisition Electronics board
613	ADC	Analog-to-Digital Converter
614	APSS	Auxiliary Payload Sensor Suite
615	C&DH	Command and Data Handling unit

616	CTL	Control Electronics board
617	DC	Power Distribution and Conditioning Electronics board
618	DMM	Digital Multi-Meter
619	E-Box	Electronics Box
620	FIR	Finite Impulse Response filter
621	FPGA	Field Programmable Gate Array
622	FLASH	non-volatile memory
623	FM	Flight Model
624	HP <sup>3</sup>	Heat Flow and Physical Properties Package
625	INL	Integral Non-Linearity
626	InSight	Interior exploration using Seismic Investigations, Geodesy and Heat Transport
627	LOBT	Local On-Board Time
628	LVL	Leveling Structure
629	LVL-MDE	Leveling Motor Drive Electronics
630	PDDU	Power Distribution & Drive Unit
631	PDS	Planetary Data System
632	RISE	Rotation and Interior Structure Experiment
633	RWEB	Remote Warm Enclosure Box
634	SCIT	Scientific Temperature
635	SCLK	Spacecraft Clock
636	SEIS	Seismic Experiment for Interior Structure
637	SA	Sensor Assembly
638	SP	Short Period sensors
639	SP-FB	SP Feedback board

640 UTC Universal Time Coordinated

641 VBB Very-Broadband sensors

642 VBB-FB VBB Feedback board

643 WEB Warm Electronics Box

644 WTS Wind and Thermal Shield

645

646 *Data and Resources – see detailed information below*

647 *Tick-Noise Removal Implementation in MATLAB and PYTHON code*

648 The function TICKREM is provided in MATLAB and PYTHON code, available for download in  
649 the electronic supplement to this article. It reads a mini seed file, corrects it and writes another

650 mini seed file. For mini seed read and write, the MATLAB version calls the functions

651 RDMSEED and MKMSEED, downloadable from MathWorks web site

652 [[https://ch.mathworks.com/matlabcentral/fileexchange/28803-rdmseed-and-mkmseed-read-and-](https://ch.mathworks.com/matlabcentral/fileexchange/28803-rdmseed-and-mkmseed-read-and-write-miniseed-files)  
653 [write-miniseed-files](https://ch.mathworks.com/matlabcentral/fileexchange/28803-rdmseed-and-mkmseed-read-and-write-miniseed-files)].

654 The read and write file names and corresponding directory paths can be specified in the  
655 arguments. The stacking and the removal process is performed in double precision floating point,  
656 but rounded to integer before writing to the mini seed file. The result is written to the same  
657 SEED compression format as read (Note: only Steim1 and Steim2 are implemented).

658 There are three other arguments that control the correction function. The argument [hp\_filt] sets  
659 the corner frequency of the first-order high-pass filter in Hz. The value [0] will switch-off the  
660 filter, the recommended default value is [0.1] Hz. The argument [var\_threshold] defines the  
661 threshold that defines up to which variance level the waveform chunk is used for the stacking  
662 process. Chunks with a variance level higher than [var\_threshold] are disregarded (refer to  
663 section [Tick-noise removal]). The recommended default value is [ $10^{+05}$ ]. Finally, the argument

[dither], which further reduces the residual of the tick-noise by applying and thus randomizing the waveform. The recommended value is [1.0], which corresponds to a dither of  $\pm 0.5$  count. The value set to zero will switch-off the dither.

The default values are suitable for most waveforms.

The InSight mission raw and calibrated data sets are available via NASA's Planetary Data System (PDS; National Aeronautics and Space Administration Planetary Data System, <https://pds.nasa.gov/>; InSight Mars SEIS Data Service (2019)). Data are delivered to the PDS according to the InSight Data Management Plan available in the InSight PDS archive. All datasets can be accessed at <https://pds-geosciences.wustl.edu/missions/insight/index.html>.

## *Acknowledgments*

We acknowledge NASA, CNES and its partner agencies and institutions (UKSA, SSO, DLR, JPL, IPGP-CNRS, ETHZ, IC and MPS-MPG) and the flight operations team at JPL, SISMOC, MSDS, IRIS-DMC and PDS for providing SEIS data. The Swiss co-authors were jointly funded by (1) the Swiss National Science Foundation and French Agence Nationale de la Recherche (SNF-ANR project 157133 'Seismology on Mars'), (2) the Swiss National Science Foundation (SNF project 172508 'Mapping the internal structure of Mars'), (3) the Swiss State Secretariat for Education, Research and Innovation, (4) ETH research grant ETH-06 17-2. This is InSight contribution number 208.

## *References*

Banerdt, W. B., S. Smrekar, D. Banfield, D. Giardini, M. Golombek, C. Johnson, P. Lognonné, A. Spiga, T. Spohn, C. Perrin, S. Stähler, D. Antonangeli, S. Asmar, C. Beghein, N.

Bowles, E. Bozdag, P. Chi, U. Christensen, J. Clinton, G. Collins, I. Daubar, V. Dehant,  
 M. Drilleau, M. Fillingim, B. Folkner, R. Garcia, J. Garvin, J. Grant, M. Grott, J.  
 Grygorczuk, T. Hudson, J. Irving, G. Kargl, T. Kawamura, S. Kedar, S. King, B.  
 Knapmeyer-Endrun, M. Knapmeyer, M. Lemmon, R. Lorenz, J. Maki, L. Margerin, S.  
 McLennan, C. Michaut, D. Mimoun, A. Mittelholz, A. Mocquet, P. Morgan, N. Mueller,  
 S. N. Murdoch, Nagihara, C. Newman, F. Nimmo, M. Panning, T. Pike, A.-C. Plesa, S.  
 Rodriguez, J.-A. Rodriguez-Manfredi, C. Russell, N. Schmerr, M. Siegler, S. Stanley, E.  
 Stutzmann, N. Teanby, J. Tromp, M. van Driel, N. Warner, R. Weber, and M. Wieczorek,  
 Initial results from the InSight mission on Mars. *Nat. Geosci.* 13, 183–189 (2020).  
<https://doi.org/10.1038/s41561-020-0544-y>

Banfield, D., J.A. Rodriguez-Manfredi, C.T. Russell, K.M. Rowe, D. Leneman, H.R. Lai, P.R.  
 Cruce, J.D. Means, C.L. Johnson, S.P. Joy, P.J. Chi, I.G. Mikellides, S. Carpenter, S.  
 Navarro, E. Sebastian, J. Gomez-Elvira, J. Torres, L. Mora, V. Peinado, A. Lepinette, K.  
 Hurst, P. Lognonné, S.E. Smrekar and W.B. Banerdt, InSight Auxiliary Payload Sensor  
 Suite (APSS). *Space Sci. Rev.* (2018). <https://doi.org/10.1007/s11214-018-0570-x>

Brinkman, N., C. Schmelzbach, D. Sollberger, M. van Driel, J. ten Pierick, J. O. A. Robertsson,  
 F. Andersson, S. Kedar, M. Grott, T. Hudson, W. B. Banerdt, L. Fayon, A. Horleston, K.  
 Hurst, A. Kiely, B. Knapmeyer-Endrun, C. Krause, P. Lognonné, W. T. Pike, S. Stähler,  
 T. Spohn, and N. Teanby (2019), The first active-seismic experiment on Mars to  
 characterize the shallow subsurface structure at the InSight landing site, SEG Technical  
 Program Expanded Abstracts 2019, 4756–4760, doi:10.1190/segam2019-3215661.1

S. Ceylan, J.F. Clinton, D. Giardini, M. Böse, C. Charalambous, M. van Driel, A. Horleston,  
T. Kawamura, A. Khan, G. Orhand-Mainsant, JR. Scholz, S. Stähler, F. Euchner,  
W.B. Banerdt, P. Lognonné, D. Banfield, E. Beucler, R.F. Garcia, S. Kedar,  
M.P. Panning, W.T. Pike, S.E. Smrekar, A. Spiga, N.L. Dahmen, K. Hurst, A.E. Stott,  
R. D. Lorenz, M. Schimmel, E. Stutzmann, J. ten Pierick, V. Conejero, C. Pardo,  
C. Perrin, (2020), Companion guide to the Marsquake catalog from InSight, sols 0–478:  
Data content and non-seismic events, Physics of the Earth and Planetary Interiors.  
<https://doi.org/10.1016/j.pepi.2020.106597>

Folkner, W.M., V. Dehant, S. Le Maistre, M. Yseboodt, A. Rivoldini, T. Van Hoolst, S.W.  
Asmar, M.P. Golombek, The Rotation and Interior Structure Experiment on the InSight  
Mission to Mars, Space Sci. Rev., 214:100, 2018. doi:10.1007/s11214-018-0530-5

Golombek, M., M. Grott, G. Kargl, J. Andrade, J. Marshall, N. Warner, N.A. Teanby, V. Ansan,  
E. Hauber, J. Voigt, R. Lichtenheldt, B. Knapmeyer-Endrun, I.J. Daubar, D. Kipp, N.  
Muller, P. Lognonné, C. Schmelzbach, D. Banfield, A. Trebi-Ollennu, J. Maki, S. Kedar,  
D. Mimoun, N. Murdoch, S. Piqueux, P. Delage, W.T. Pike, C. Charalambous, R.  
Lorenz, L. Fayon, A. Lucas, S. Rodriguez, P. Morgan, A. Spiga, M. Panning, T. Spohn,  
S. Smrekar, T. Gudkova, R. Garcia, D. Giardini, U. Christensen, T. Nicollier, D.  
Sollberger, J. Robertsson, K. Ali, B. Kenda and W. B. Banerdt (2018), Geology and  
Physical Properties Investigations by the InSight Lander, Space Science Review, 214(5),  
84, 10.1007/s11214-018-0512-7.



735 Kedar, S., Andrade, J., Banerdt, B., Delage, P., Golombek, M., Grott, M., T. Hudson, A. Kiely,  
 736 M. Knapmeyer, B. Knapmeyer-Endrun, C. Krause, T. Kawamura, P. Lognonné,  
 737 W.T. Pike, Y. Ruan, T. Spohn, N. Teanby, J. Tromp and J. Wookey (2017). Analysis of  
 738 Regolith Properties Using Seismic Signals Generated by InSight's HP<sup>3</sup> Penetrator. Space  
 739 Science Reviews, 211, 315–337. doi: 10.1007/s11214-017-0391-3  
 740  
 741 P. Lognonné, W.B. Banerdt, D. Giardini, W.T. Pike, U. Christensen, P. Laudet, S. de Raucourt,  
 742 P. Zweifel, S. Calcutt, M. Bierwirth, K.J. Hurst, F. Ijpelaan, J.W. Umland, R. Llorca-  
 743 Cejudo, S.A. Larson, R.F. Garcia, S. Kedar, B. Knapmeyer-Endrun, D. Mimoun, A.  
 744 Mocquet, M.P. Panning, R.C. Weber, A. Sylvestre-Baron, G. Pont, N. Verdier, L.  
 745 Kerjean, L.J. Facto, V. Gharakanian, J.E. Feldman, T.L. Hoffman, D.B. Klein, K. Klein,  
 746 N.P. Onufer, J. Paredes-Garcia, M.P. Petkov, J.R. Willis, S.E. Smrekar, M. Drilleau, T.  
 747 Gabsi, T. Nebut, O. Robert, S. Tillier, C. Moreau, M. Parise, G. Aveni, S. Ben Charef, Y.  
 748 Bennour, T. Camus, P.A. Dandonneau, C. Desfoux, B. Lecomte, O. Pot, P. Revuz,  
 749 D. Mance, J. tenPierick, N.E. Bowles, C. Charalambous, A.K. Delahunty, J. Hurley, R.  
 750 Irshad, H. Liu, A.G. Mukherjee, I.M. Standley, A.E. Stott, J. Temple, T. Warren, M.  
 751 Eberhardt, A. Kramer, W. Kühne, E.-P. Miettinen, M. Monecke, C. Aicardi, M. André, J.  
 752 Baroukh, A. Borrien, A. Bouisset, P. Boutte, K. Brethomé, C. Brysbaert, T. Carlier, M.  
 753 Deleuze, J.M. Desmarres, D. Dilhan, C. Doucet, D. Faye, N. Faye-Refalo, R. Gonzalez,  
 754 C. Imbert, C. Larigauderie, E. Locatelli, L. Luno, J.-R. Meyer, F. Mialhe, J.M. Mouret,  
 755 M. Nonon, Y. Pahn, A. Paillet, P. Pasquier, G. Perez, R. Perez, L. Perrin, B. Pouilloux, A.  
 756 Rosak, I. Savin de Larclause, J. Sicre, M. Sodki, N. Toulemont, B. Vella, C. Yana, F.  
 757 Alibay, O.M. Avalos, M.A. Balzer, P. Bhandari, E. Blanco, B.D. Bone, J.C. Bousman, P.  
 758 Bruneau, F.J. Calef, R.J. Calvet, S.A. D'Agostino, G. de los Santos, R.G. Deen, R.W.

759 Denise, J. Ervin, N.W. Ferraro, H.E. Gengl, F. Grinblat, D. Hernandez, M. Hetzel, M.E.  
 760 Johnson, L. Khachikyan, J.Y. Lin, S.M. Madzunkov, S.L. Marshall, I.G. Mikellides, E.A.  
 761 Miller, W. Raff, J.E. Singer, C.M. Sunday, J.F. Villalvazo, M.C. Wallace, D. Banfield,  
 762 J.A. Rodriguez-Manfredi, C.T. Russell, A. Trebi-Ollennu, J.N. Maki, E. Beucler, M.  
 763 Böse, C. Bonjour, J.L. Berenguer, S. Ceylan, J. Clinton, V. Conejero, I. Daubar, V.  
 764 Dehant, P. Delage, F. Euchner, I. Estève, L. Fayon, L. Ferraioli, C.L. Johnson, J.  
 765 Gagnepain-Beyneix, M. Golombek, A. Khan, T. Kawamura, B. Kenda, P. Labrot, N.  
 766 Murdoch, C. Pardo, C. Perrin, L. Pou, A. Sauron, D. Savoie, S. Stähler, E. Stutzmann,  
 767 N.A. Teanby, J. Tromp, M. van Driel, M. Wieczorek, R. Widmer-Schmidrig, J. Wookey  
 768 (2019). SEIS: Insight's seismic experiment for internal structure of Mars.  
 769 <https://doi.org/10.1007/s11214-018-0574-6>  
 770  
 771 Lognonné, P., W. B. Banerdt, W. T. Pike, D. Giardini, U. Christensen, R. F. Garcia, T.  
 772 Kawamura, S. Kedar, B. Knapmeyer-Endrun, L. Margerin, F. Nimmo, M. Panning, B.  
 773 Tauzin, J. R. Scholz, D. Antonangeli, S. Barkaoui, E. Beucler, F. Bissig, N. Brinkman,  
 774 M. Calvet, S. Ceylan, C. Charalambous, P. Davis, M. van Driel, M. Drilleau, L. Fayon,  
 775 R. Joshi, B. Kenda, A. Khan, M. Knapmeyer, V. Lekic, J. McClean, D. Mimoun, N.  
 776 Murdoch, L. Pan, C. Perrin, B. Pinot, L. Pou, S. Menina, S. Rodriguez, C. Schmelzbach,  
 777 N. Schmerr, D. Sollberger, A. Spiga, S. Stähler, A. Stott, E. Stutzmann, S. Tharimena, R.  
 778 Widmer-Schmidrig, F. Andersson, V. Ansan, C. Beghein, M. Böse, E. Bozdog, J. Clinton,  
 779 I. Daubar, P. Delage, N. Fuji, M. Golombek, M. Grott, A. Horleston, K. Hurst, J. Irving,  
 780 A. Jacob, J. Knollenberg, S. Krasner, C. Krause, R. Lorenz, C. Michaut, B. Myhill, T.  
 781 Nissen-Meyer, J. ten Pierick, A.-C. Plesa, C. Quantin-Nataf, J. Robertsson, L. Rochas, M.  
 782 Schimmel, S. Smrekar, T. Spohn, N. Teanby, J. Tromp, J. Vallade, N. Verdier, C.

Vrettos, R. Weber, D. Banfield, E. Barrett, M. Bierwirth, S. Calcutt, N. Compaire, C. Johnson, D. Mance, F. Euchner, L. Kerjean, G. Mainsant, J. A. Rodriguez Manfredi, G. Pont, P. Laudet, T. Nebut, S. de Raucourt, O. Robert, C. Russell, A. Sylvestre-Baron, S. Tillier, T. Warren, M. Wieczorek, C. Yana, P. Zweifel, Constraints on the shallow elastic and anelastic structure of Mars from InSight seismic data. Nat. Geosci., 13, 213–220 (2020). <https://doi.org/10.1038/s41561-020-0536-y>

Scholz, J.- R., R. Widmer-Schmidrig, P. Davis, P. Lognonné, B. Pinot, R. F. Garcia, F. Nimmo, K. Hurst, S. Barkaoui, S. de Raucourt, L. Pou, B. Pinot, N. Compaire, G. Mainsant, A. Cuvier, E. Beucler, M. Bonnin, R. Joshi, E. Stutzmann, M. Schimmel, A. Horleston, M. Böse, S. Ceylan, J. Clinton, M. van Driel, T. Kawamura, A. Khan, S. C. Stähler, D. Giardini, C. Charalambous, A. E. Stott, W. T. Pike, U. Christensen and W. B. Banerdt (2020). Detection, analysis and removal of glitches from InSight’s seismic data from Mars. Earth and Space Science 7, e2020EA001317- T. <https://doi.org/10.1029/2020EA001317>

Spohn, T., M. Grott, S. E. Smrekar, J. Knollenberg, T. L. Hudson, C. Krause, N. Müller. J. Jänchen, A. Börner, T. Wippermann, O. Krömer, R. Lichtenheldt, L. Wisniewski, J. Grygorczuk, M. Fittock, S. Reershemius, T. Sprowitz, E. Kopp, I. Walter, A.-C. Plesa, D. Breuer, P. Morgan, W. B. Banerdt, The Heat Flow and Physical Properties Package (HP<sup>3</sup>) for the InSight Mission, Space Sci. Rev., 214:96, 2018. <https://doi.org/10.1007/s11214-018-0531-4>

806 Sollberger, D., C. Schmelzbach, F. Andersson, J. O. A. Robertsson, S. Kedar, W. B. Banerdt, N.  
807 Brinkman, J. Clinton, M. van Driel, R. Garcia, D. Giardini, M. Grott, T. Haag, T. L.  
808 Hudson, P. Lognonné, J. ten Pierick, W. T. Pike, T. Spohn, S. Stähler, P. Zweifel, (2020),  
809 Reconstruction of temporally aliased seismic signals recorded by the InSight Mars lander,  
810 submitted to Earth and Space Science, 10.1002/essoar.10502908.1  
811  
812 InSight Mars SEIS Data Service. (2019). SEIS raw data, Insight Mission. IPGP, JPL, CNES,  
813 ETHZ, ICL, MPS, ISAE-Supaero, LPG, MFSC.  
814 [https://doi.org/10.18715/SEIS.INSIGHT.XB\\_2016](https://doi.org/10.18715/SEIS.INSIGHT.XB_2016)  
815  
816 NASA InSight Web Site. Artist's rendering of the Sensor Assembly. Credit: NASA/JPL-  
817 Caltech/CNES/IPGP Download on [https://mars.nasa.gov/resources/22107/cutaway-of-](https://mars.nasa.gov/resources/22107/cutaway-of-seis/?site=insight)  
818 [seis/?site=insight](https://mars.nasa.gov/resources/22107/cutaway-of-seis/?site=insight)

*Full mailing address for each author*

W. Bruce	Banerdt	<a href="mailto:william.b.banerdt@jpl.nasa.gov">william.b.banerdt@jpl.nasa.gov</a>	Jet Propulsion Laboratory / California Institute of Technology	4800 Oak Grove Drive	Pasadena, CA 91109	USA
Marco	Bierwirth	<a href="mailto:bierwirthm@mps.mpg.de">bierwirthm@mps.mpg.de</a>	Max-Planck-Institute for Solar System Research, Göttingen	Justus-von-Liebig Weg 3	D-37077 Göttingen	Germany
Savas	Ceylan	<a href="mailto:savas.ceylan@erdw.ethz.ch">savas.ceylan@erdw.ethz.ch</a>	Eidgenössische Technische Hochschule Zürich / Institute of Geophysics	Sonneggstrasse 5	CH-8092 Zurich	Switzerland
John F.	Clinton	<a href="mailto:jclinton@sed.ethz.ch">jclinton@sed.ethz.ch</a>	Eidgenössische Technische Hochschule Zürich / Swiss Seismological Service	Sonneggstrasse 5	CH-8092 Zurich	Switzerland
Michel	Eberhardt	<a href="mailto:eberhardt@mps.mpg.de">eberhardt@mps.mpg.de</a>	Max-Planck-Institute for Solar System Research, Göttingen	Justus-von-Liebig Weg 3	D-37077 Göttingen	Germany
Fabian	Euchner	<a href="mailto:fabian.euchner@sed.ethz.ch">fabian.euchner@sed.ethz.ch</a>	Eidgenössische Technische Hochschule Zürich / Swiss Seismological Service	Sonneggstrasse 5	CH-8092 Zurich	Switzerland
Domenico	Giardini	<a href="mailto:domenico.giardini@erdw.ethz.ch">domenico.giardini@erdw.ethz.ch</a>	Eidgenössische Technische Hochschule Zürich / Institute of Geophysics	Sonneggstrasse 5	CH-8092 Zurich	Switzerland
Thomas	Haag	<a href="mailto:thomas.haag@erdw.ethz.ch">thomas.haag@erdw.ethz.ch</a>	Eidgenössische Technische Hochschule Zürich / Institute of Geophysics	Sonneggstrasse 5	CH-8092 Zurich	Switzerland
Philippe	Lognonné	<a href="mailto:lognonne@ipgp.fr">lognonne@ipgp.fr</a>	Institut de Physique du Globe de Paris	35 rue Hélène Brion	75205 Paris Cedex 13	France
Davor	Mance	<a href="mailto:davor.mance@retired.ethz.ch">davor.mance@retired.ethz.ch</a>	Eidgenössische Technische Hochschule Zürich / Institute of Geophysics	Sonneggstrasse 5	CH-8092 Zurich	Switzerland
Tobias	Nicollier	<a href="mailto:tobias.nicollier@wsl.ch">tobias.nicollier@wsl.ch</a>	Eidgenössische Forschungsanstalt WSL	Zürcherstrasse 111	CH-8903 Birmensdorf	Switzerland
William T.	Pike	<a href="mailto:w.t.pike@ic.ac.uk">w.t.pike@ic.ac.uk</a>	Imperial College London	Exhibition Road	London SW7 2AZ	United Kingdom
Cedric	Schmelzbach	<a href="mailto:cedric.schmelzbach@erdw.ethz.ch">cedric.schmelzbach@erdw.ethz.ch</a>	Eidgenössische Technische Hochschule Zürich / Institute of Geophysics	Sonneggstrasse 5	CH-8092 Zurich	Switzerland
David	Sollberger	<a href="mailto:david.sollberger@erdw.ethz.ch">david.sollberger@erdw.ethz.ch</a>	Eidgenössische Technische Hochschule Zürich / Institute of Geophysics	Sonneggstrasse 5	CH-8092 Zurich	Switzerland

Simon	Stähler	<a href="mailto:simon.staehler@erdw.ethz.ch">simon.staehler@erdw.ethz.ch</a>	Eidgenössische Technische Hochschule Zürich / Institute of Geophysics	Sonneggstrasse 5	CH-8092 Zurich	Switzerland
Jan	ten Pierick	<a href="mailto:jan.tenpierick@erdw.ethz.ch">jan.tenpierick@erdw.ethz.ch</a>	Eidgenössische Technische Hochschule Zürich / Institute of Geophysics	Sonneggstrasse 5	CH-8092 Zurich	Switzerland
Martin	van Driel	<a href="mailto:vandriel@erdw.ethz.ch">vandriel@erdw.ethz.ch</a>	Eidgenössische Technische Hochschule Zürich / Institute of Geophysics	Sonneggstrasse 5	CH-8092 Zurich	Switzerland
Peter	Zweifel	<a href="mailto:peter.zweifel@retired.ethz.ch">peter.zweifel@retired.ethz.ch</a>	Eidgenössische Technische Hochschule Zürich / Institute of Geophysics	Sonneggstrasse 5	CH-8092 Zurich	Switzerland

822 *Tables, with captions above each table*

823

824 *List of Figure Captions*

825 Figure 1 Artist’ rendering showing a cutaway of the SEIS Sensor Assembly (SA) and the Wind  
826 and Thermal Shield (WTS). The leveling structure (LVL) was delivered by Max-Planck Solar  
827 System Research in Göttingen, Germany (MPS), the VBB sensor by the Institut du Physique du  
828 Globe in Paris, France, the SP sensors by Imperial College in London, UK, and the Wind and  
829 Thermal Shield (WTS) and tether by Jet Propulsion Laboratory (JPL) in Pasadena, USA. Credit:  
830 NASA/JPL-Caltech/CNES/IPGP (NASA InSight Web Site)..... 41

831 Figure 2 SEIS Electronics Box (E-Box) outside view, physical configuration and electrical  
832 interconnections. The picture upper left shows the Flight Model (FM) unit, in preparation for the  
833 thermal test. Dimensions: 244 mm (height), 170 mm (width), 344 mm (length); weight ~5 kg; E-  
834 Box was delivered by ETH Zurich in Switzerland. The exploded view of the E-Box shows the  
835 board configuration: three VBB-FB feedback boards (delivered by IPGP); one SP-FB feedback  
836 board (delivered by Oxford University); one motor drive electronic board LVL-MDE (delivered  
837 by MPS); one ACQ acquisition board (partially duplicated) and two duplicated control  
838 electronics boards CTL; two duplicated DC power boards, condition the primary +28 V to all  
839 secondary voltages needed by the sub-systems (delivered by ETHZ). Figure credit to Syderal  
840 SA, Switzerland, the manufacturer of the E-Box. The Block Diagram (lower part of the figure)  
841 shows the interconnections within the SEIS instrument and to the external units Command &  
842 Data Handling C&DH, the Power Distribution and Drive Unit PDDU and the Auxiliary Payload  
843 Sensor Suite APSS (Banfield, 2018) ..... 42

844	Figure 3 Acquisition chain with the anti-alias filter steps (block diagram on top). The charts	
845	show the attenuation of the individual filters (left) and the attenuation combined (right) for the	
846	velocity chain at 20 Hz output rate. ....	43
847	Figure 4 FIR filter stages for the VBB and SP velocity channels (upper diagram) and for the	
848	VBB position and scientific temperature (SCIT) channels (lower diagram).....	44
849	Figure 5 Acquisition Noise Breakdown of VBB velocity channel. (P. Lognonné, 2019).....	45
850	Figure 6 Noise Performance of VBB channels, compared to the acquisition system noise. VBB	
851	position channels (left chart) at a sample rate of 1 Hz; recordings from 2019-10-18 at 20:00 for	
852	59 min on Mars and recordings obtained at board level test on 2014-10-04 for 59 min. VBB	
853	velocity channels (right chart) at a sample rate of 100 Hz; recordings from 2020-02-04 at 17:52	
854	for 15 min on Mars (event and recordings obtained at board level test on 2014-10-16 for 15 min	
855	.....	45
856	Figure 7 Noise Performance of SP velocity channels during cruise and on Mars, compared to the	
857	acquisition system noise; sample rate = 100 Hz; recordings from 2019-01-12 at 05:10 for 15 min	
858	on Mars, from 2018-07-16 at 15:48 for 7 min during cruise, and recordings obtained at board	
859	level test on 2014-10-16 for 15 min.....	46
860	Figure 8 Linearity Measurement: Principal configuration (block diagram) and measurement	
861	results .....	47
862	Figure 9 Scientific Temperature (SCIT A) time-series and ASD, measured on a fixed resistor	
863	instead of a thermistor. Sampling rate = 1 Hz; 2 h time-series; this measurement has been	
864	performed in the final test campaign of E-Box FM before delivery to CNES for SEIS integration.	
865	.....	48
866	Figure 10 Sampling strategy to record signals with frequencies up to 100 Hz (simulating a	
867	sampling rate of 200 Hz from two separate 100 Hz recordings). (Upper row) The VBB data will	



868	be acquired with the standard anti-alias filter (0–50 Hz low-pass filter) when down-sampling the	
869	signals digitized at 500 Hz to 100 Hz. (Lower row) The SP data will be filtered with a 50–100	
870	Hz band pass filter, which results in the SP data being folded one time. For the reconstruction of	
871	the 0–100 Hz bandwidth (corresponding to 200 Hz sampling; see rightmost sketch), the aliased	
872	SP data are folded back before adding the VBB and SP data together. Due to the periodicity of	
873	the Fourier transform, down-sampling to 100 Hz will cause the signal to be periodically repeated	
874	along the frequency axis at a spacing of 100 Hz (so-called aliases). The different filters used for	
875	the SP and VBB channels ensure that the aliases do not overlap, so that they can be individually	
876	isolated and used for the reconstruction.....	48
877	Figure 11 The drift of the LOBT versus the SCLK in the second reporting period from 2019-10-	
878	14 to 2020-10-05.....	49
879	Figure 12 Left side: Amplitude spectra of SP1, SP2 and SP3 channels at high gain and 20 Hz	
880	sampling rate; 24 h time-series; start time 2020-08-29 00:00:00 UTC; tick-noise amplitudes	
881	calculated from the samples of the stacked signal: SP1= 7.2 $\mu$ Vrms, SP2 = 3.9 $\mu$ Vrms, SP3 = 7.4	
882	$\mu$ Vrms. Right side: Amplitude spectra of VBB1, VBB2 and VBB3 channels in high gain and 20	
883	Hz data rate; 40 min time-series; start time at 2020-07-04 14:50:00; tick-noise amplitudes	
884	calculated from the samples of the stacked signal: VBB1 = 7.5 $\mu$ Vrms, VBB2 = 49.2 $\mu$ Vrms,	
885	VBB3 =14.2 $\mu$ Vrms.....	50
886	Figure 13 Left side: Stacked waveforms for SP1, SP2 and SP3 at high gain and 20 Hz sampling	
887	rate; recordings from 2019-07-22 (18 hours), from 2020-01-03 (48 hours) and from 2020-08-28	
888	(24 hours). Right side: Stacked waveforms for VBB1, VBB2 and VBB3; recordings from 2019-	
889	06-04 (48 hours), 2020-01-03 (48 hours) and 2020-07-04 (48 hours) .....	51
890	Figure 14 Comparison of the stacked waveform, SP1, recorded on 2019-01-12 at 05:07:26 for 48	
891	min, with 100 Hz sample rate, high-pass filter with 0.1 Hz corner frequency; left: all available	

data is stacked, right: variance level set to  $10^4$  counts; 328 of 2880 1-second chunks were rejected..... 52

Figure 15 Corrected SP1 data, high-pass filter with 0.1 Hz corner frequency, accepting waveform chunks for the stacking process only with a variance below variance level  $10^4$  counts, as in Figure 14 on the right side. Data recorded on 2019-01-12 at 05:07:26 for 48 min, with 100 Hz sample rate. .... 52

*Figures, with captions below each figure – high resolution figure files are not needed for the review process. They will be requested after your paper is accepted for publication.*

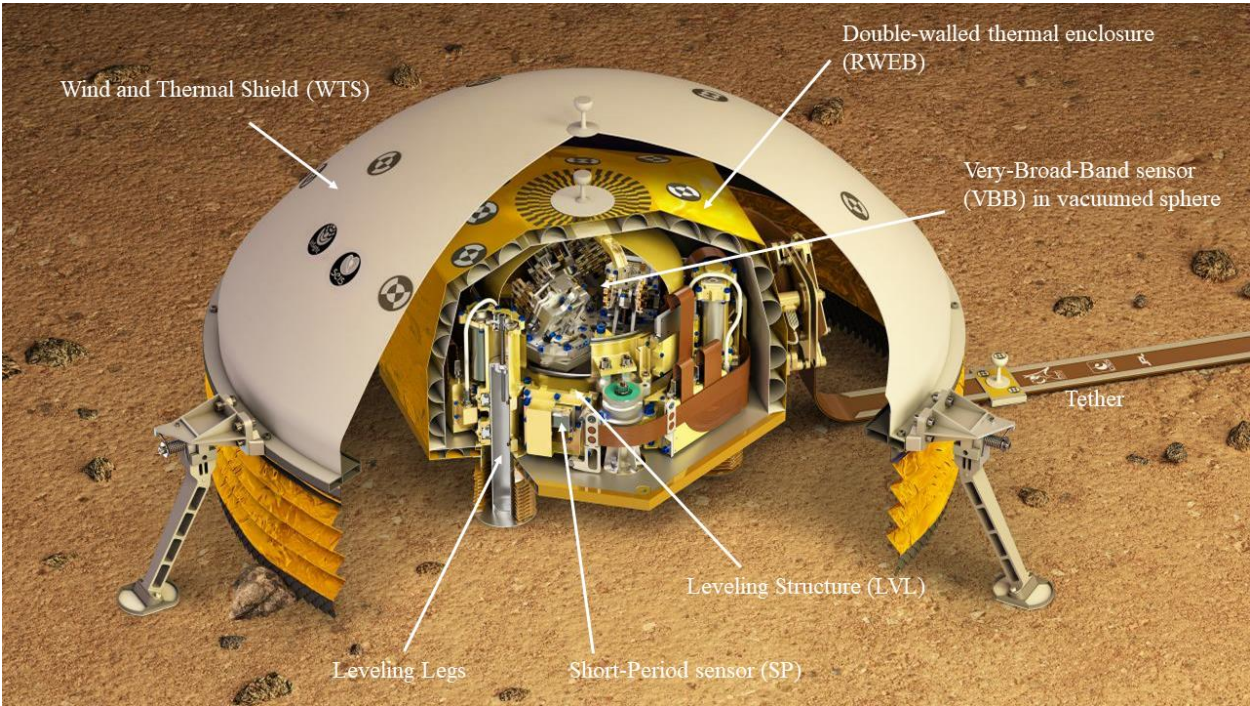


Figure 1 Artist' rendering showing a cutaway of the SEIS Sensor Assembly (SA) and the Wind and Thermal Shield (WTS). The leveling structure (LVL) was delivered by Max-Planck Solar System Research in Göttingen, Germany (MPS), the VBB sensor by the Institut du Physique du Globe in Paris, France, the SP sensors by Imperial College in London, UK, and the Wind and Thermal Shield (WTS) and tether by Jet Propulsion Laboratory (JPL) in Pasadena, USA. Credit: NASA/JPL-Caltech/CNES/IPGP (NASA InSight Web Site)

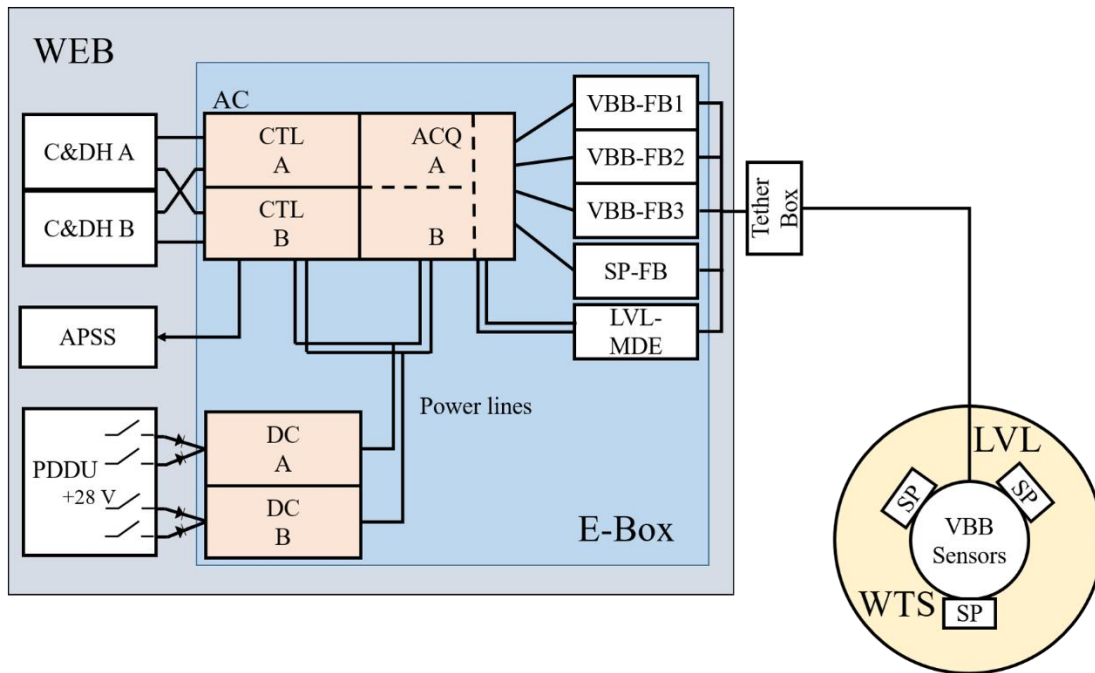
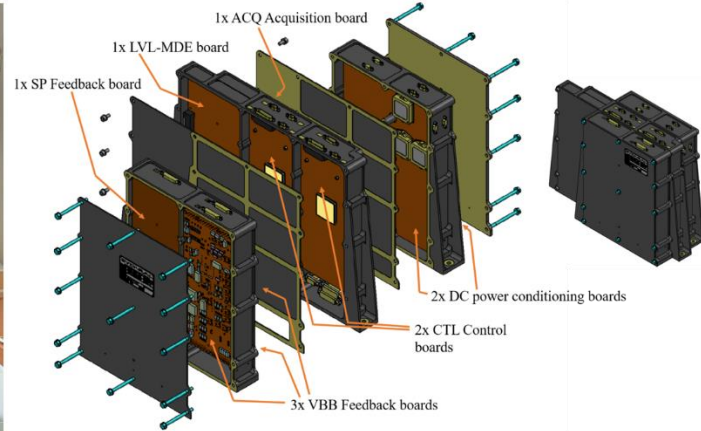
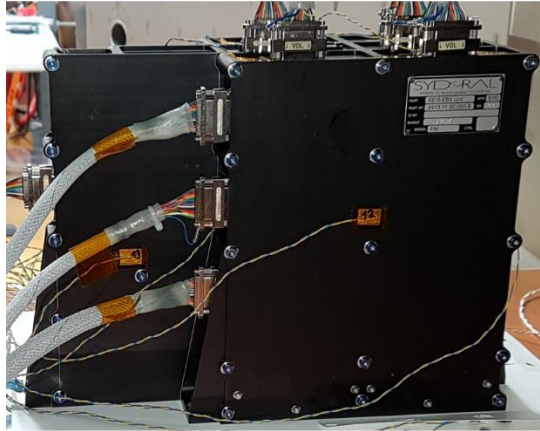


Figure 2 SEIS Electronics Box (E-Box) outside view, physical configuration and electrical interconnections. The picture upper left shows the Flight Model (FM) unit, in preparation for the thermal test. Dimensions: 244 mm (height), 170 mm (width), 344 mm (length); weight ~5 kg; E-Box was delivered by ETH Zurich in Switzerland. The exploded view of the E-Box shows the board configuration: three VBB-FB feedback boards (delivered by IPGP); one SP-FB feedback board (delivered by Oxford University); one motor drive electronic board LVL-MDE (delivered by MPS); one ACQ acquisition board (partially duplicated) and two duplicated control electronics boards CTL; two duplicated DC power boards, condition the primary +28 V to all secondary voltages needed by the sub-systems (delivered by ETHZ). Figure credit to Syderal SA, Switzerland, the manufacturer of the E-Box. The Block Diagram (lower part of the figure) shows the interconnections within the SEIS instrument and to the external units Command & Data Handling C&DH, the Power Distribution and Drive Unit PDDU and the Auxiliary Payload Sensor Suite APSS (Banfield, 2018)

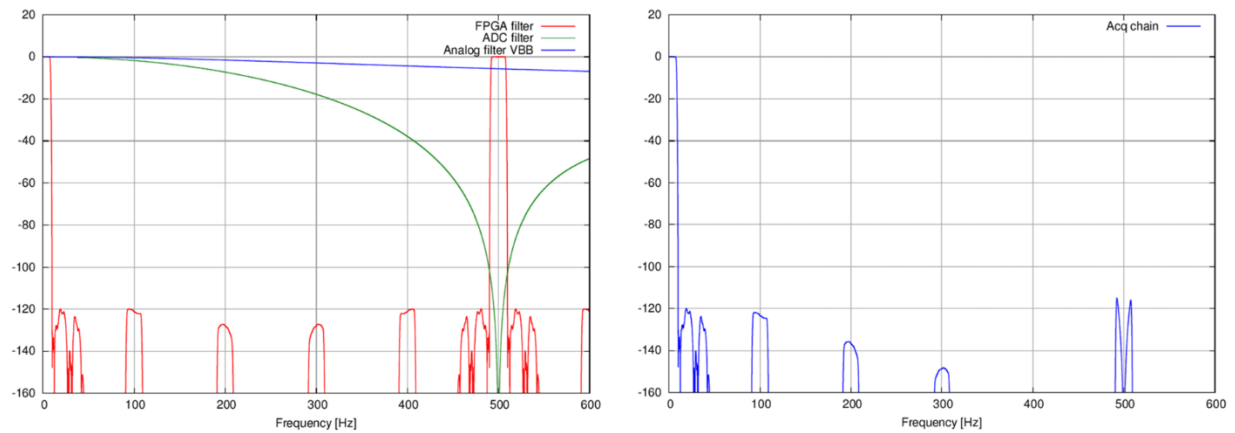
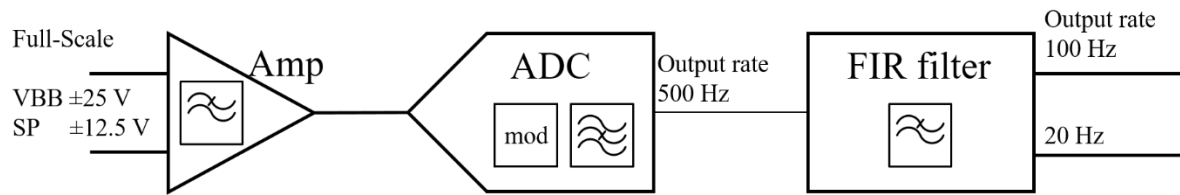


Figure 3 Acquisition chain with the anti-alias filter steps (block diagram on top). The charts show the attenuation of the individual filters (left) and the attenuation combined (right) for the velocity chain at 20 Hz output rate.

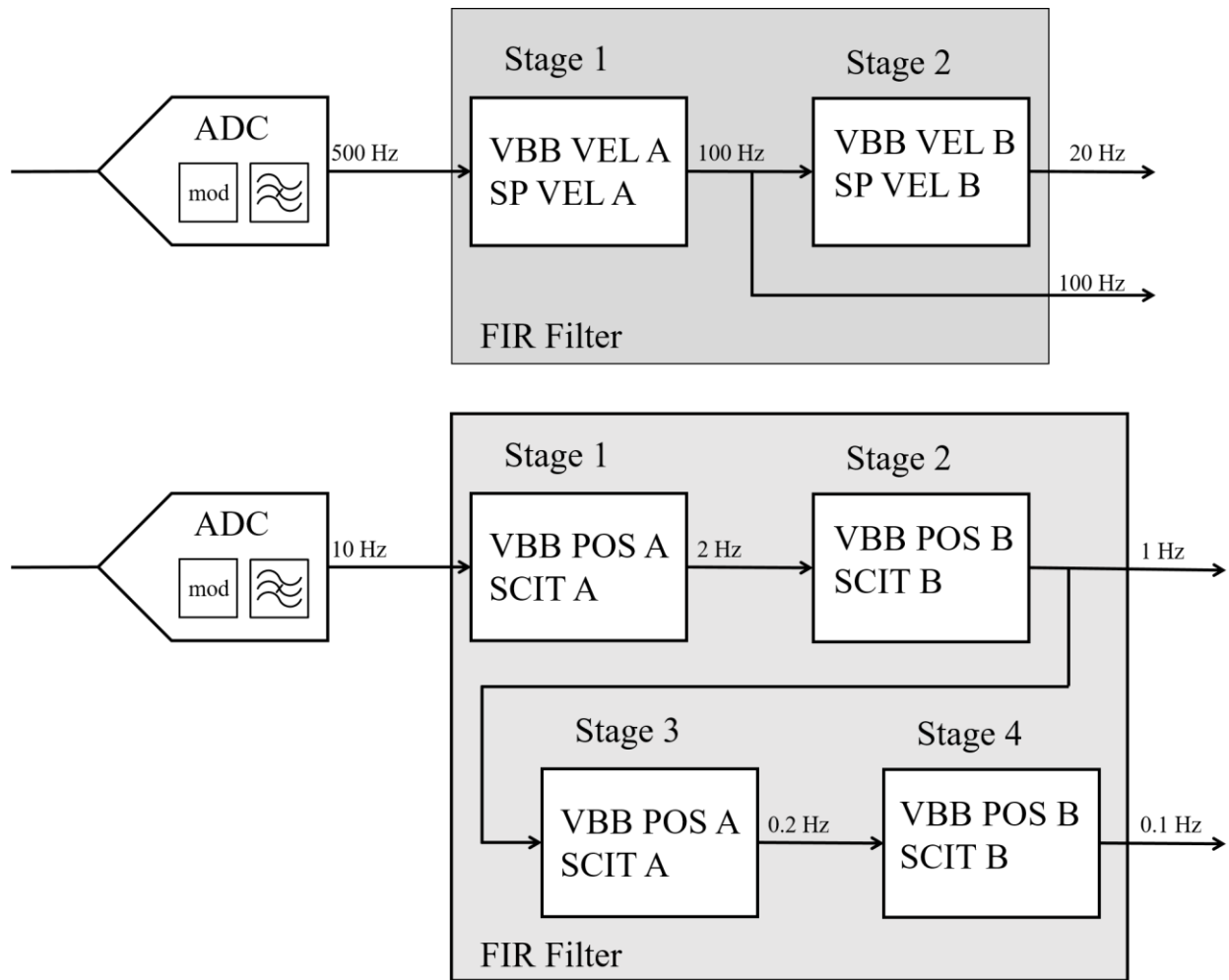


Figure 4 FIR filter stages for the VBB and SP velocity channels (upper diagram) and for the VBB position and scientific temperature (SCIT) channels (lower diagram)



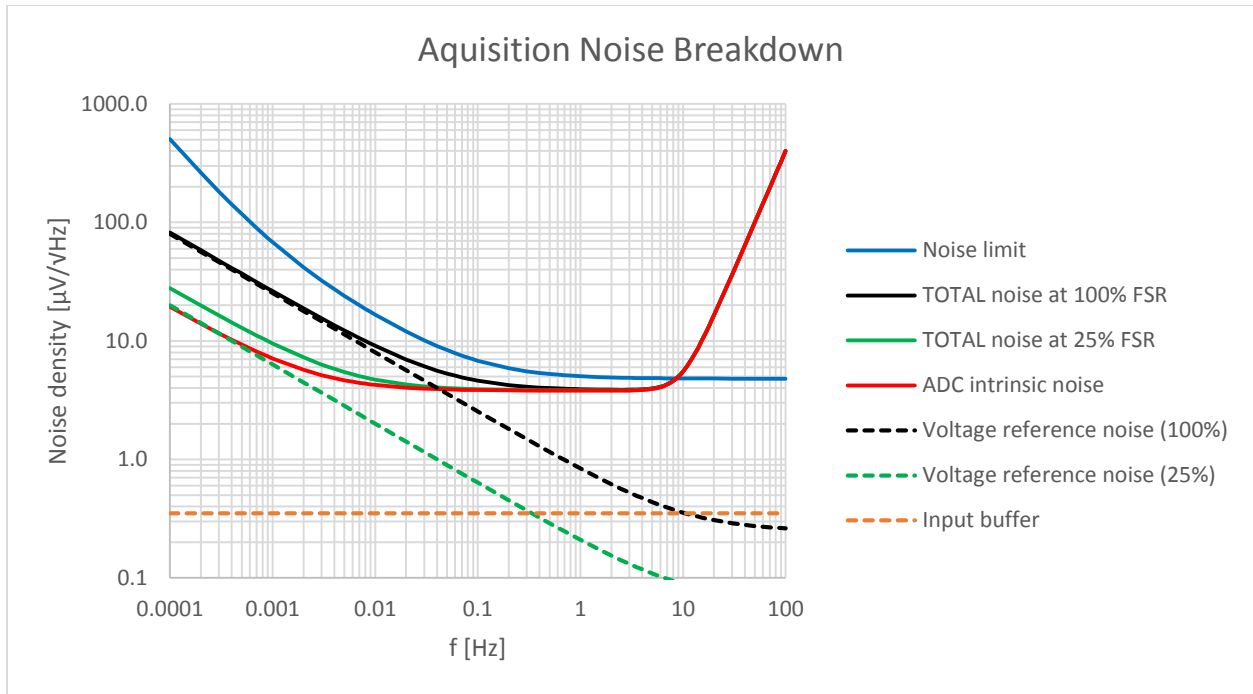


Figure 5 Acquisition Noise Breakdown of VBB velocity channel. (P. Lognonné, 2019)

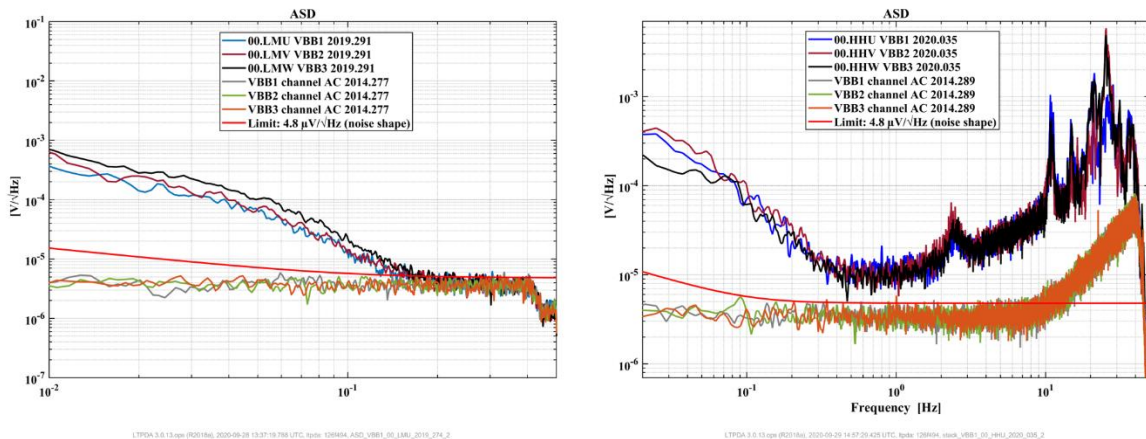
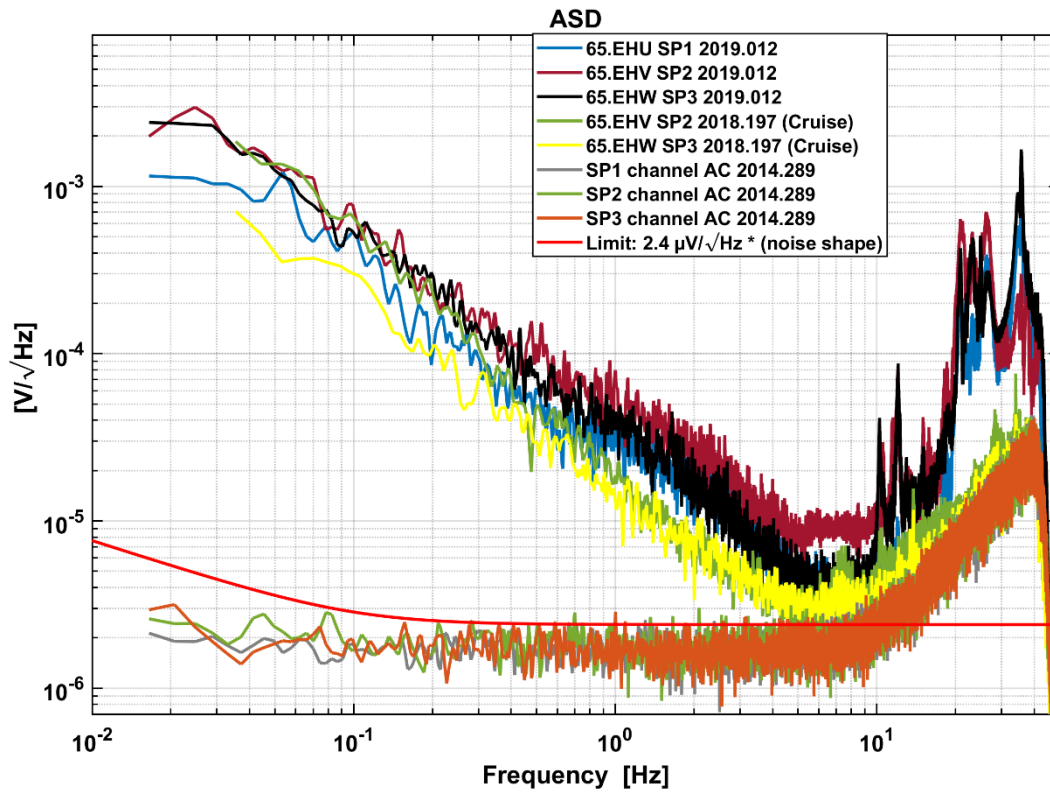


Figure 6 Noise Performance of VBB channels, compared to the acquisition system noise. VBB position channels (left chart) at a sample rate of 1 Hz; recordings from 2019-10-18 at 20:00 for 59 min on Mars and recordings obtained at board level test on 2014-10-04 for 59 min. VBB velocity channels (right chart) at a sample rate of 100 Hz; recordings from 2020-02-04 at 17:52 for 15 min on Mars (event and recordings obtained at board level test on 2014-10-16 for 15 min



LTPDA 3.0.13 ops (R2018a), 2020-09-27 11:11:43.892 UTC, ltpda: 126f494, stack\_SP1\_65\_EHU\_2019\_012\_1

Figure 7 Noise Performance of SP velocity channels during cruise and on Mars, compared to the acquisition system noise; sample rate = 100 Hz; recordings from 2019-01-12 at 05:10 for 15 min on Mars, from 2018-07-16 at 15:48 for 7 min during cruise, and recordings obtained at board level test on 2014-10-16 for 15 min

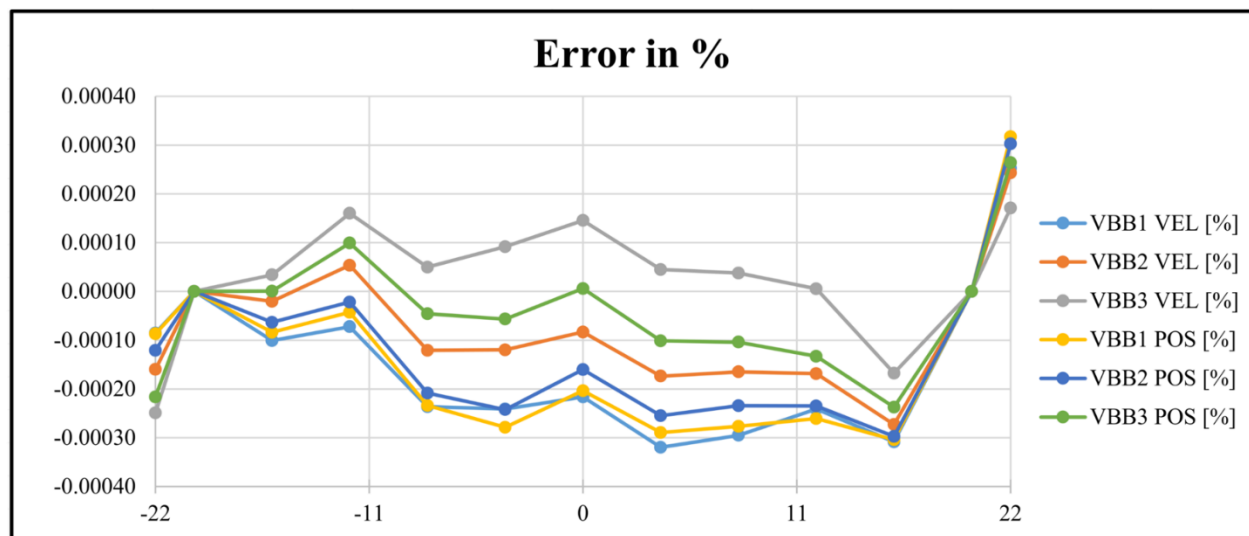
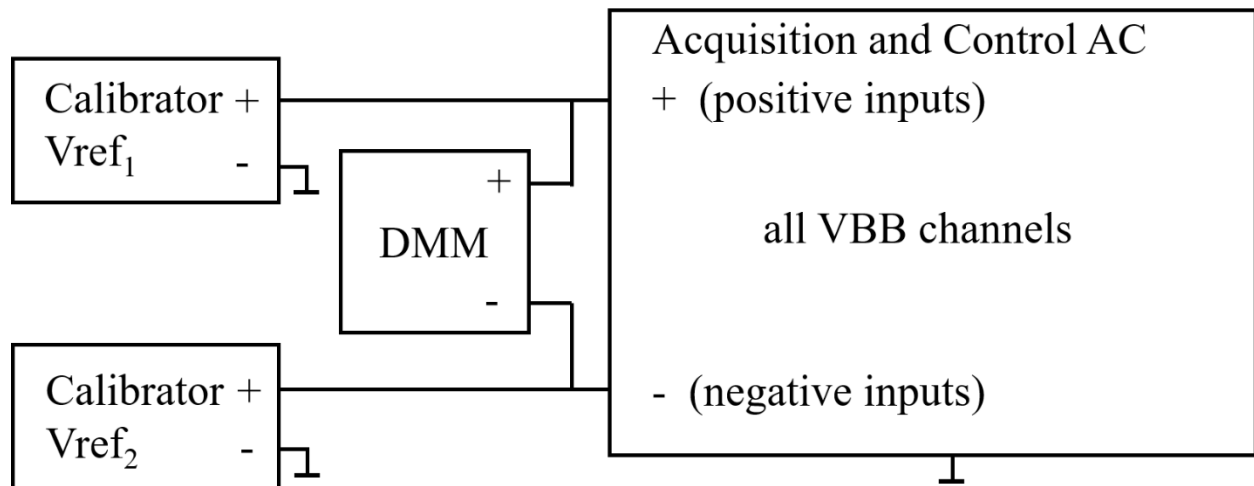


Figure 8 Linearity Measurement: Principal configuration (block diagram) and measurement results



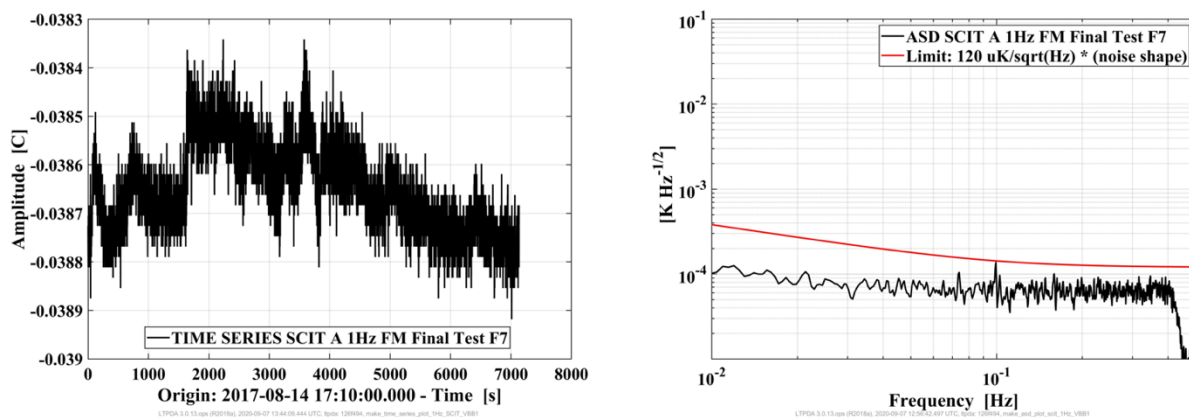


Figure 9 Scientific Temperature (SCIT A) time-series and ASD, measured on a fixed resistor instead of a thermistor. Sampling rate = 1 Hz; 2 h time-series; this measurement has been performed in the final test campaign of E-Box FM before delivery to CNES for SEIS integration.

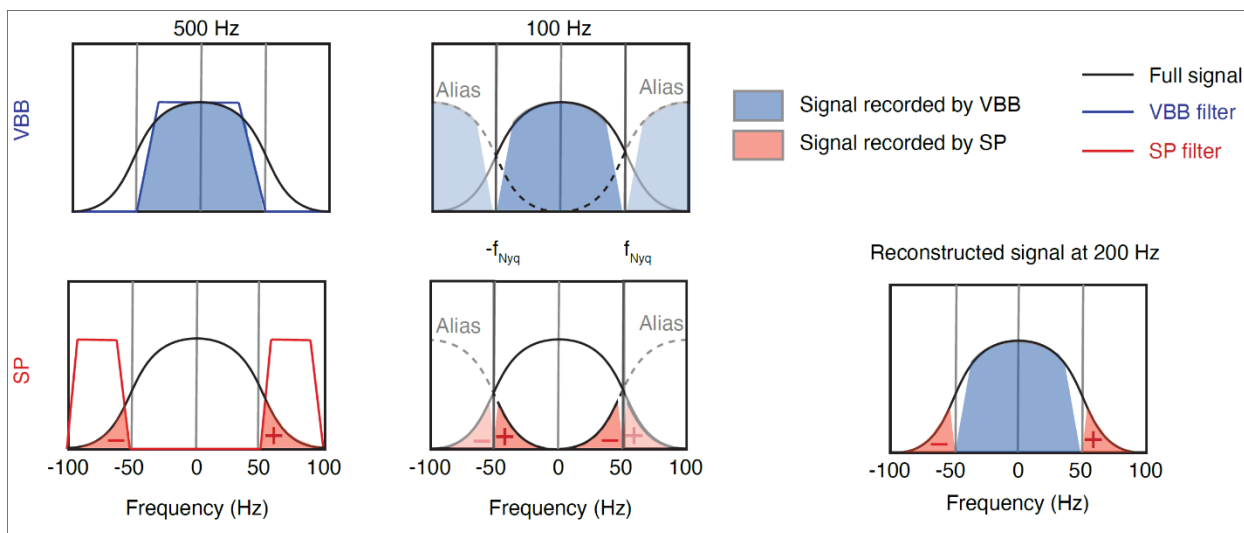


Figure 10 Sampling strategy to record signals with frequencies up to 100 Hz (simulating a sampling rate of 200 Hz from two separate 100 Hz recordings). (Upper row) The VBB data will be acquired with the standard anti-alias filter (0–50 Hz low-pass filter) when down-sampling the signals digitized at 500 Hz to 100 Hz. (Lower row) The SP data will be filtered with a 50–100 Hz band pass filter, which results in the SP data being folded one time. For the reconstruction of the 0–100 Hz bandwidth (corresponding to 200 Hz sampling; see rightmost sketch), the aliased SP data are folded back before adding the VBB and SP data together. Due to the periodicity of the Fourier transform, down-sampling to 100 Hz will cause the signal to be periodically repeated along the frequency axis at a spacing of 100 Hz (so-called aliases). The different filters used for the SP and VBB channels ensure that the aliases do not overlap, so that they can be individually isolated and used for the reconstruction.

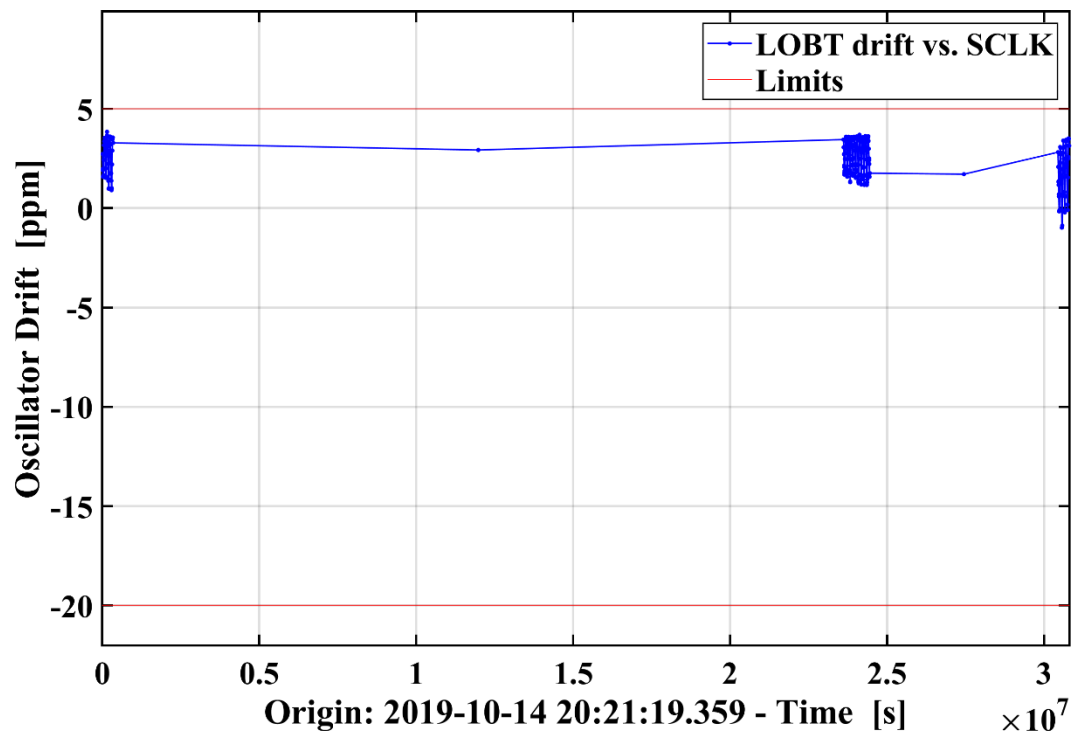


Figure 11 The drift of the LOBT versus the SCLK in the second reporting period from 2019-10-14 to 2020-10-05

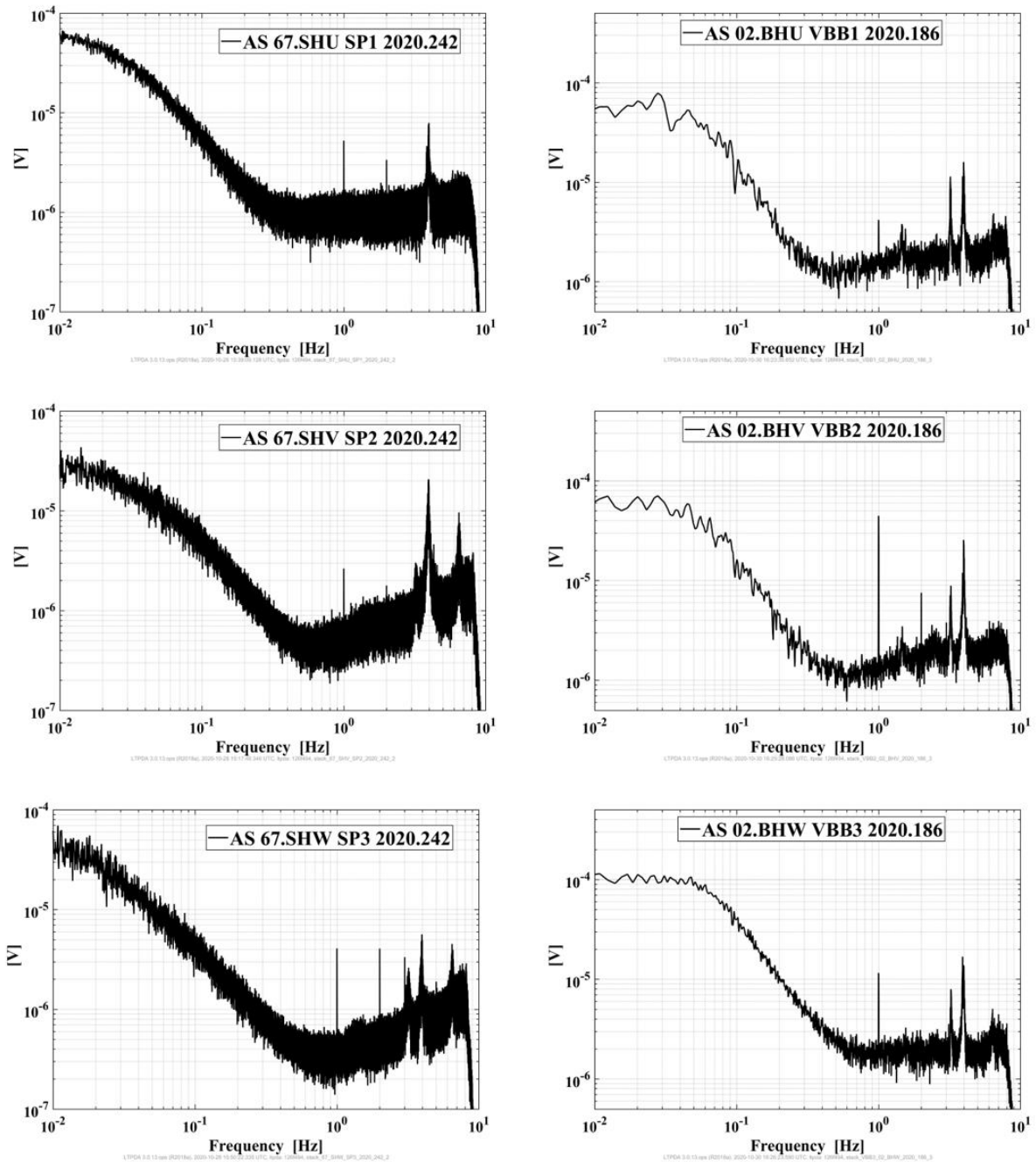


Figure 12 Left side: Amplitude spectra of SP1, SP2 and SP3 channels at high gain and 20 Hz sampling rate; 24 h time-series; start time 2020-08-29 00:00:00 UTC; tick-noise amplitudes calculated from the samples of the stacked signal: SP1= 7.2  $\mu$ Vrms, SP2 = 3.9  $\mu$ Vrms, SP3 = 7.4  $\mu$ Vrms. Right side: Amplitude spectra of VBB1, VBB2 and VBB3 channels in high gain and 20 Hz data rate; 40 min time-series; start time at 2020-07-04 14:50:00; tick-noise amplitudes calculated from the samples of the stacked signal: VBB1 = 7.5  $\mu$ Vrms, VBB2 = 49.2  $\mu$ Vrms, VBB3 =14.2  $\mu$ Vrms

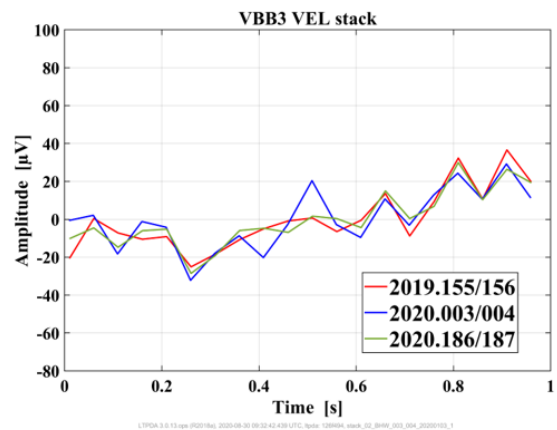
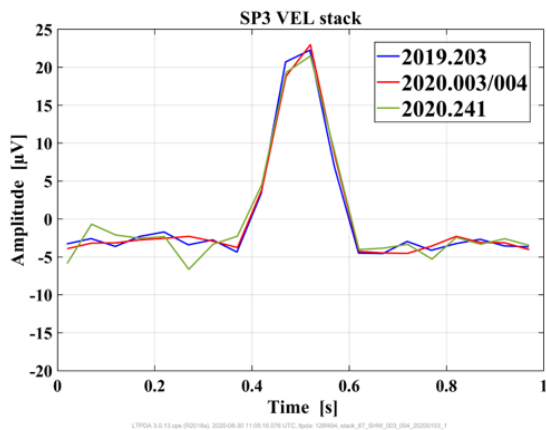
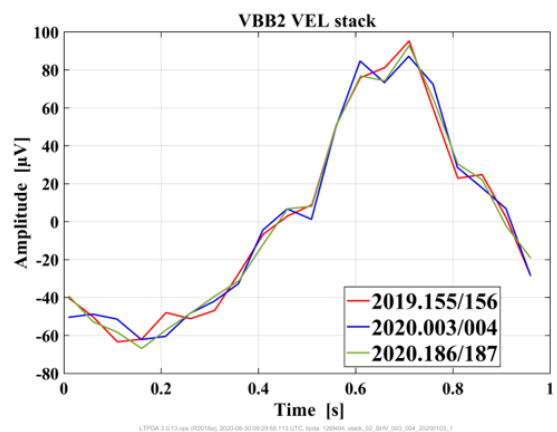
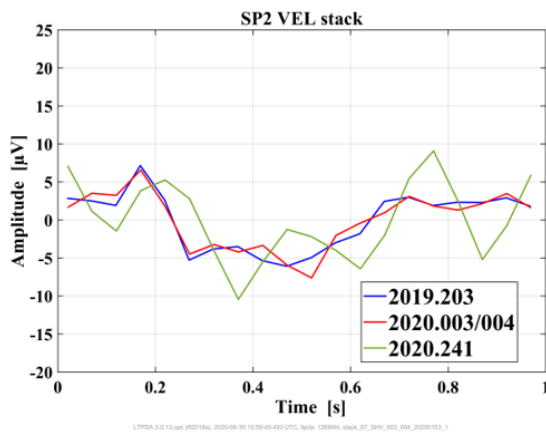
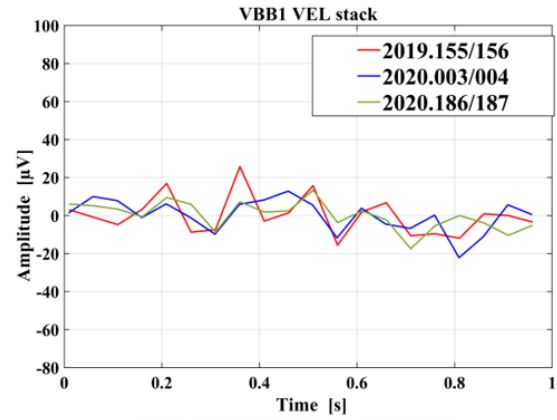
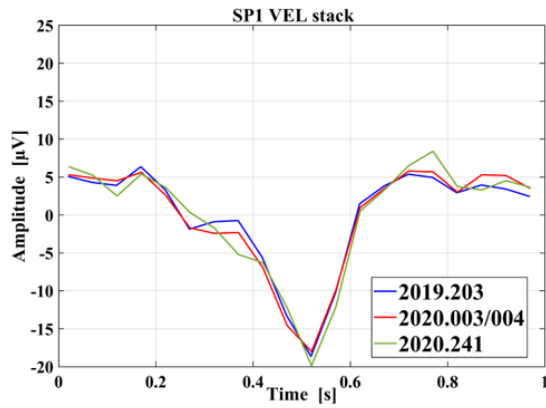


Figure 13 Left side: Stacked waveforms for SP1, SP2 and SP3 at high gain and 20 Hz sampling rate; recordings from 2019-07-22 (18 hours), from 2020-01-03 (48 hours) and from 2020-08-28 (24 hours). Right side: Stacked waveforms for VBB1, VBB2 and VBB3; recordings from 2019-06-04 (48 hours), 2020-01-03 (48 hours) and 2020-07-04 (48 hours)

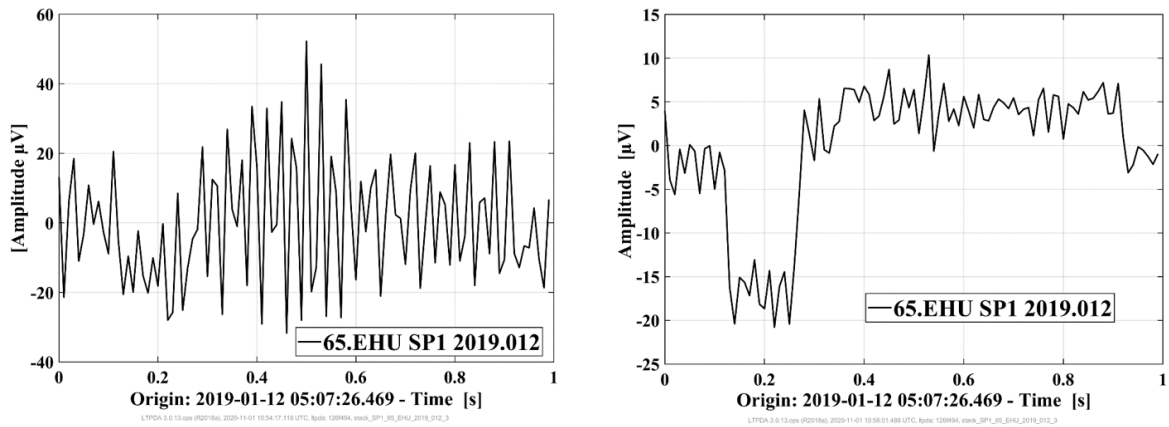


Figure 14 Comparison of the stacked waveform, SP1, recorded on 2019-01-12 at 05:07:26 for 48 min, with 100 Hz sample rate, high-pass filter with 0.1 Hz corner frequency; left: all available data is stacked, right: variance level set to  $10^4$  counts; 328 of 2880 1-second chunks were rejected

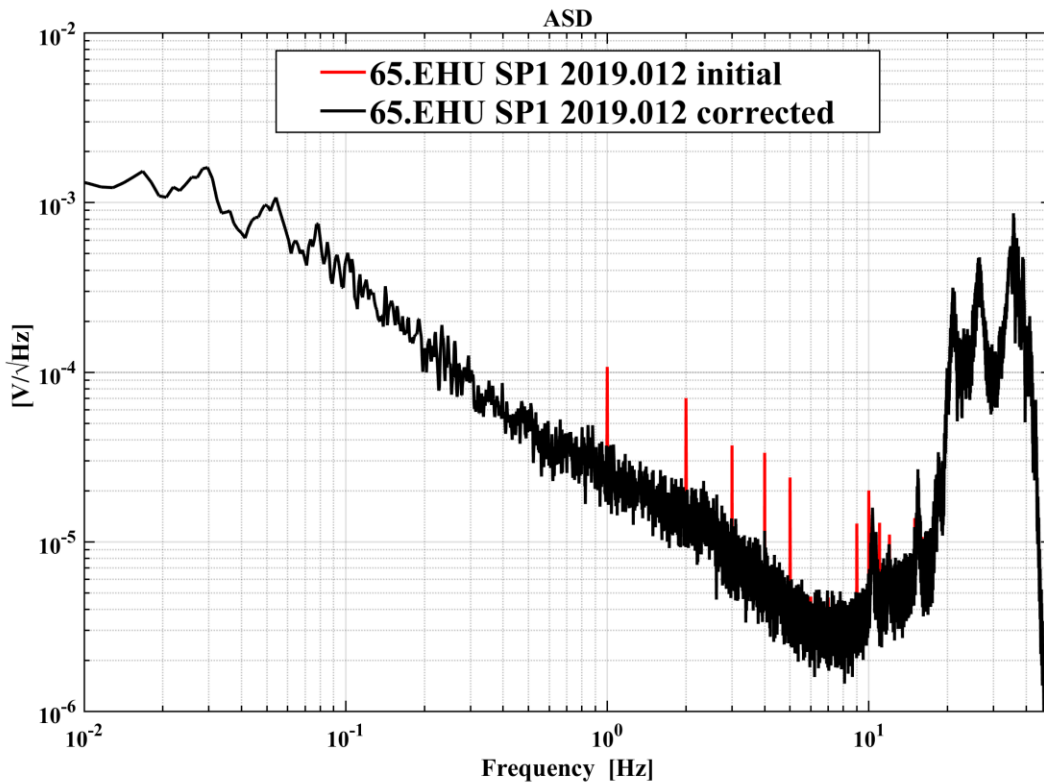


Figure 15 Corrected SP1 data, high-pass filter with 0.1 Hz corner frequency, accepting waveform chunks for the stacking process only with a variance below variance level  $10^4$  counts, as in Figure 14 on the right side. Data recorded on 2019-01-12 at 05:07:26 for 48 min, with 100 Hz sample rate.

1001 *Appendices (optional)* – equations, figures and tables labeled using “A” (i.e. Table  
1002 A1, A2; Figure A1, A2; Eq. A1, A2, etc.)  
1003 Electronic Supplement (optional) – Authors may submit supplemental digital material  
1004 to accompany papers. See [Electronic Supplement Guidelines](#) for further instructions.  
1005 If your paper has an electronic supplement, include citations for this material in the  
1006 text (i.e. “for a complete list of earthquakes, see Table S4 in the electronic supplement  
1007 to this article.”)  
1008



[Click here to access/download](#)

**Supplemental Material (All Other Files, i.e. Movie, Zip,  
tar)**

MATLAB\_tickrem\_20201221.zip





[Click here to access/download](#)

**Supplemental Material (All Other Files, i.e. Movie, Zip,  
tar)**

PYTHON\_tickrem\_20210225.zip

